Unravelling the complex sub-ice geology of the Wilkes Subglacial Basin region of East Antarctica from marine sediment provenance analyses

MAYURI PANDEY[1], NARESH CHANDRA PANT [2], DEVSAMRIDHI ARORA[3], FAUSTO FERRACCIOLI[4], RASHMI GUPTA[1] and SONALIKA JOSHI[5]

[1]*Banaras Hindu University, Varanasi, India*
[2]*Department of Geology, University of Delhi, Delhi, India*
[3]*National Centre of Experimental Mineralogy and Petrology, University of Allahabad, Allahabad, India*
[4]*National Institute of Oceanography and Applied Geophysics - OGS, Sgonico (TS), Italy*
[5]*Geological Survey of India, Jaipur, India*
pantnc@gmail.com

Abstract: Deciphering the sub-ice geology in the Wilkes Subglacial Basin region is important for understanding solid earth-ice sheet evolution and for assessing geological ties between East Antarctica and formerly contiguous Australia. We analyse marine sediment samples derived from drill site U1359 of Integrated Oceanic Drilling Program Expedition 318. Our study reports for the first time that the inland sediment source area comprises a complex mafic igneous terrain and a metamorphosed Precambrian subglacial basement. Pyroxene geochemical analyses confirm the presence of tholeiitic to calc-alkaline basalts. The high-grade part of the subglacial terrain contains upper amphibolite to granulite facies rocks that are comparable to Archaean to Palaeoproterozoic rocks exposed in the Terre Adélie Craton and the formerly adjacent Gawler Craton in Australia. Chemical Th-U-total Pb isochron method (CHIME) ages extracted from a subhedral monazite grain associated with the low-grade biotite-muscovite schist rock fragment provide a unimodal age of 799 ± 13 Ma. Rare occurrences of 800 Ma age in the Terre Adélie Craton and/or George V Coast provide evidence for the presence of at least one late Neoproterozoic magmato-metamorphic event in the interior of Wilkes Land. The affinity of the unexposed geological domains of Wilkes Land, East Antarctica, with their Australian counterparts is discussed in the context of the Rodinia supercontinent.

Introduction

Australo-Antarctica comprises several geophysically distinct Precambrian crustal domains. Various attempts were made to reconstruct the Precambrian basement geology of Antarctica and Australia based on the continuity of comparable geological terranes, major shear zones and geophysical signatures (e.g. Aitken *et al.* 2016). However, the paucity of knowledge regarding regional variations in sub-ice geology within the composite East Antarctic Craton (e.g. Harley *et al.* 2013) continues to hamper determinations of the extent of Australian geological entities in the interior of the Antarctic Wilkes Land terrain.

Gleaning an improved understanding of the subglacial geology in East Antarctica is also critical for the development of new models and reconstructions to assess the stability of the East Antarctic Ice Sheet (EAIS) within future warmer climate scenarios (e.g. DeConto *et al.* 2007, Pollard & DeConto 2009, 2016, Pollard *et al.* 2015). The Wilkes Subglacial Basin (WSB) sector of East Antarctica is of particular importance for assessments of past and future EAIS stability (Fig. 1; e.g. Ferraccioli *et al.* 2009, Pandey *et al.* 2021). The bedrock beneath the WSB lies mostly below sea level, and in several regions the bedrock deepens inland, making this sector of East Antarctica potentially more prone to marine ice-sheet instability processes. However, the development of robust models of past EAIS behaviour requires validation through both geophysical and geological datasets.

Our knowledge of the subglacial geology and topography in Wilkes Land has improved significantly due to aero geophysical surveys such as the International Collaborative Exploration of the Cryosphere through Airborne Profiling Project (ICECAP; e.g. Aitken *et al.* 2014, Frederick *et al.* 2016) and Icehouse Earth: Stability or Dynamism/Wilkes Basin/Transantarctic
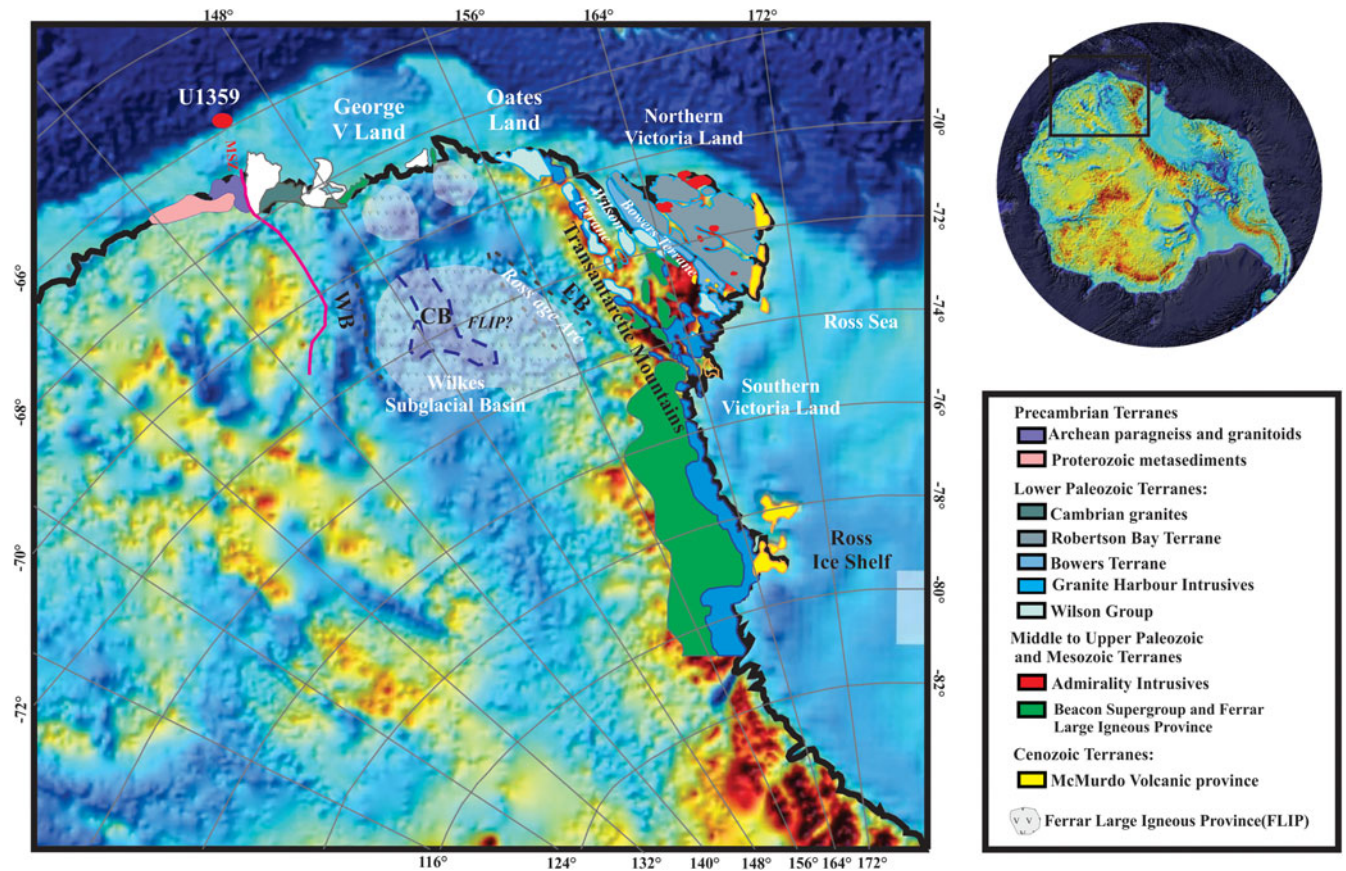
Fig. 1. Geological map of exposed bedrock around East Antarctica in proximity to Wilkes Land (inferred by Ferraccioli *et al.* 2009, Cook *et al.* 2013) displayed over a subglacial bedrock topography map (from Bedmap2; Fretwell *et al.* 2013) to indicate probable sediment provenance areas for the sediments we investigated at site U1359 of Integrated Oceanic Drilling Program Expedition 318. CB = Central Basin; EB = Eastern Basin; MSZ = Mertz Shear Zone; WB = Western Basin.

Mountains System Exploration (ISODYN/WISE; e.g. Ferraccioli *et al.* 2009, Jordan *et al.* 2010). However, the inferences from geophysical methods still require further confirmation and verification through direct geological evidence to directly probe and identify hidden geological terranes.

Linkage of the Wilkes Land sector of East Antarctica and its Australian counterpart based on the geophysical and geological inferences from coastal exposures suggest the presence of large-scale Palaeoproterozoic basements accreted during supercontinent reassembly (Aitken *et al.* 2016). The Wilkes Land sector itself can be divided into three components: 1) the west Wilkes province occupies the region west of the Totten Glacier from Windmill Islands to the west of Law Dome comprising Sabrina Subglacial Basin (Morrissey *et al.* 2017), 2) central Wilkes Land from the Totten Glacier to the Mertz Suture Zone comprising Frost Subglacial Basin and Astrolabe Subglacial Basin (Aitken *et al.* 2014) and 3) eastern Wilkes Land with WSB, which predominantly comprises Archaean to Palaeoproterozoic rocks exposed in Terre Adélie Land and George V Land and has geological

affinities with the Gawler Craton of South Australia (Fitzsimons 2003, Aitken *et al.* 2014). However, these inferences are mostly from the unconstrained projection of the Australian geological terrain in the interior of the Wilkes Land terrain. These projections are unable to infer the presence of Ferrar Large Igneous Province (FLIP) in the WSB, which is suggested to be Jurassic in age purely constrained from the projection of Ferrar dolerites present in the Transantarctic Mountains (Cook *et al.* 2013).

Direct evidence of the regional geological constraints from the Wilkes sector is missing, which would be significant for understanding its thermo-tectonic history and sub-ice geological provinces. In Australo-Antarctic reconstruction, the Mertz Shear Zone (MSZ; Fig. 1) is a ~1500 Ma old mid-crustal shear zone (Lamarque *et al.* 2016, Pierce *et al.* 2017) that has been inferred to align with the Kalinjala Shear Zone (KSZ) in South Australia (e.g. Reid & Hand 2012). However, alternative Gondwana reconstructions favour linking the MSZ to the Coorong Shear Zone further to the east (Gibson *et al.* 2013). There is a limited rock outcrop exposed east
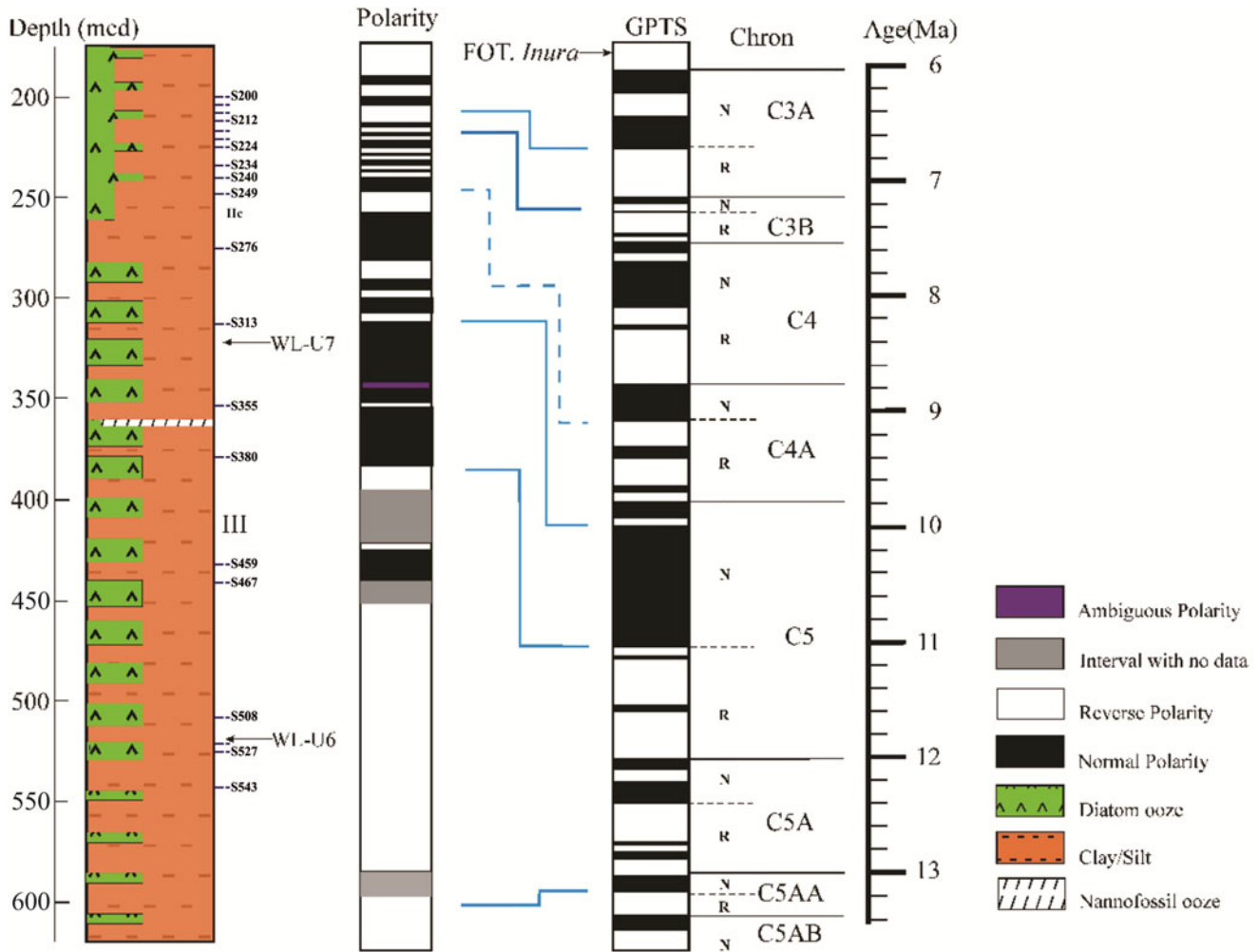
Fig. 2. A composite lithology of site U1359 (modified after Tauxe *et al.* 2012) along with age constraints based on magnetostratigraphy and biostratigraphy. Lithostratigraphic units IIc and III representing Miocene sediments of the studied cores are also mentioned. The lithostratigraphic units are based on the observed change in facies association. WL-U7 and WL-U6 are two seismic unconformities. Locations of samples selected for the present work are shown at different depths. FOT = first occurrence of *Thalassiosira inura* (Tauxe *et al.* 2012); GPTS = geomagnetic polarity timescale; mcd = measured compensated depth.

of the MSZ, which limits our direct knowledge of the sub-ice geology of this sector.

Marine sedimentary records recovered from the Antarctic continental margin provide the most accessible proxy information on the palaeoclimatic and tectono-thermal evolution of East Antarctica, as these sediments represent source rock domains (Pant *et al.* 2013, Gupta *et al.* 2022). Heavy mineral fractions of the marine sediments reflect provenance characteristics, and the utility of heavy minerals in provenance and process interpretation is widely recognized (e.g. Bateman & Catt 2007, Mange & Wright 2007). In addition, the influence of chemical weathering is relatively limited in Antarctica, especially post-formation of the EAIS since the Oligocene (e.g. Scher *et al.* 2011). Therefore, specific minerals and mineral

groups can be directly linked to particular domains of sub-ice provenance, and their chemical traits can imply the geology of these domains. The chemistry of various minerals, especially magmatic and metamorphic minerals, is predominantly governed by their genetic processes. Mineral compositions can thus be used to estimate physical conditions such as pressure and temperature for the rocks in the provenance. Our results provide new geological insights into correlations between East Antarctica and Australia, in particular during the Neoproterozoic, through heavy mineral fractions and rock fragments recovered from Integrated Oceanic Drilling Program (IODP) Expedition 318 by characterizing the lithologies of the Wilkes Land sector and comparing them to their Australian counterparts.

Geological overview of the area

Investigating the behaviour of the EAIS at the eastern margin of Wilkes Land was one of the major geoscientific objectives of IODP Expedition 318 (Escutia *et al.* 2011, Verma *et al.* 2014, Pandey *et al.* 2018). Recent geological interpretations derived from IODP Expedition 318 (e.g. Cook *et al.* 2013, 2017, Verma *et al.* 2014, Pandey *et al.* 2018, Biswas *et al.* 2020) augment earlier records from other Antarctic continental areas and margins indicating a relatively dynamic EAIS, especially during Late Miocene to Early/Middle Pliocene times (Naish *et al.* 2009, Verma *et al.* 2014, Pandey *et al.* 2018, 2021, Biswas *et al.* 2020). The general circulation model experiments of the Wilkes Land sector suggested that east wind drifts prevailed north of 60°S under Miocene boundary conditions, similar to today (Herold *et al.* 2011, Bijl *et al.* 2018). Hence, we could get sediments from as far as the Transantarctic Mountains (Pant *et al.* 2013, Cook *et al.* 2017). The proximal interior gets sediments transported mainly through Mertz and Ninnis glaciers contributing from the interior of Wilkes Land (McMullen *et al.* 2006, Orejola *et al.* 2014). All of the sediments and detritals further transported to the continental rise through the Jussieu submarine channel. Sites U1359 and U1361 were drilled on the eastern levee of this channel. The present work provides an account of the heavy phases and rock fragments of site U1359.

A marine sediment core was drilled from site U1359 during Expedition 318 at ~4003 m below sea level (mbsl) and ~100 km from the Antarctic shelf break. This site lies south of the Antarctic Polar Front and gets sediment supply through Jussieu submarine channel streams (Escutia *et al.* 2011). Because of the deepwater setting of the sedimentary archive, its stratigraphic record is relatively complete (Tauxe *et al.* 2012, Hansen *et al.* 2015).

Geology of site U1359

Four boreholes (U1359A–U1359D) were drilled at depths of 193.5, 252.0, 168.7 and 602.2 m below sea floor (mbsf), respectively, at site U1359. A composite lithology of site U1359 shows the dominance of silty clay with dispersed clasts throughout the core (Fig. 2). Five distinct lithofacies and three lithostratigraphic units were defined (Escutia *et al.* 2011) based on variations in biogenic components, bioturbation and sedimentary structures, packages of silt-fine sand laminae and diatom abundance. Details of the samples under investigation are also mentioned in Fig. 2. Lithostratigraphic Unit I (0–43.5 mbsf) consists of diatom-rich silty clays with dispersed clasts including occasional foraminifer-bearing clayey silt and sandy silt. Unit II (43.5–247.1 mbsf) is composed of interbedded bioturbated diatom-bearing silty clays and olive-grey diatom-bearing silty clays (Fig. 2). The lowermost part of Unit II (~200.0–247.1 mbsf) represents sediments of 6–9 Ma age. Unit III extends from 247.1 mbsf to the bottom of the cored section at 596.3 mbsf (~9–13 Ma; Fig. 2) and comprises interbedded bioturbated diatom-bearing silty clays and laminated silty clays (Fig. 2). Clasts > 2 mm in size occur throughout all lithostratigraphic units and are mostly dispersed in nature (1% in abundance; Escutia *et al.* 2011). A study from site U1358 suggested a stable Mertz Glacier system during the Late Pleistocene and sand size supply through ice rafting (Orejola *et al.* 2014). The presence of extensive ice-rafted debris (IRD) in some portions of sites U1359 and U1361 implies an occasional weakening of the westwards-flowing Polar Current or the collapse of the continental shelf ice sheet due to warming (Cook *et al.* 2017). Sites U1359 and U1361 are drilled close to each other, hence their sharing of various sedimentological characteristics, and they are suggested to have a multi-provenance sediment supply (Pant *et al.* 2013, Cook *et al.* 2017, Pandey *et al.* 2018).

Geology of the inland sectors

The composite Terre Adélie Craton (TAC; Terre Adélie Land and George V Land) extends along the Antarctic coast between longitudes 136.4°E and 144.5°E within the Mawson craton and represents the easternmost area of the East Antarctic Shield (Fig. 1). The eastern boundary is marked by the prominent MSZ (144.3°E; Talarico & Kleinschmidt 2003), which separates the Archaean and Proterozoic basement of the TAC from the Ross-Delamerian crystalline basement including granitoids and metasediments from the Cape Webb area (Di Vincenzo *et al.* 2007). The Ross-Delamerian rocks mark the western boundary of the Ross orogen that extends eastwards into Oates Land. The western boundary is not properly defined due to a lack of rock exposures and geophysical information. Rocher X (136.4°E) is the westernmost outcrop related to the TAC. Further west, outcrops in the Windmill Islands display Archaean and Proterozoic material strongly overprinted by late Mesoproterozoic events (between 1340 and 1130 Ma; Fitzsimons 2003). The TAC exposure is restricted to hectometre to kilometre square islands and capes scattered along the coastline and to a few nunataks, mainly in the inland area of Commonwealth Bay. Farther east is Victoria Land, which is a high-grade metamorphic terrain except that the timing of peak metamorphism of terranes in the northern part has slightly younger U-Pb ages (460–500 Ma; e.g. Schüssler *et al.* 1999) than the southern portion (*c.* 480–550 Ma; e.g. Goodge 2007). The ages of the central Transantarctic Mountains are close to 480–545 Ma (Goodge 2007).
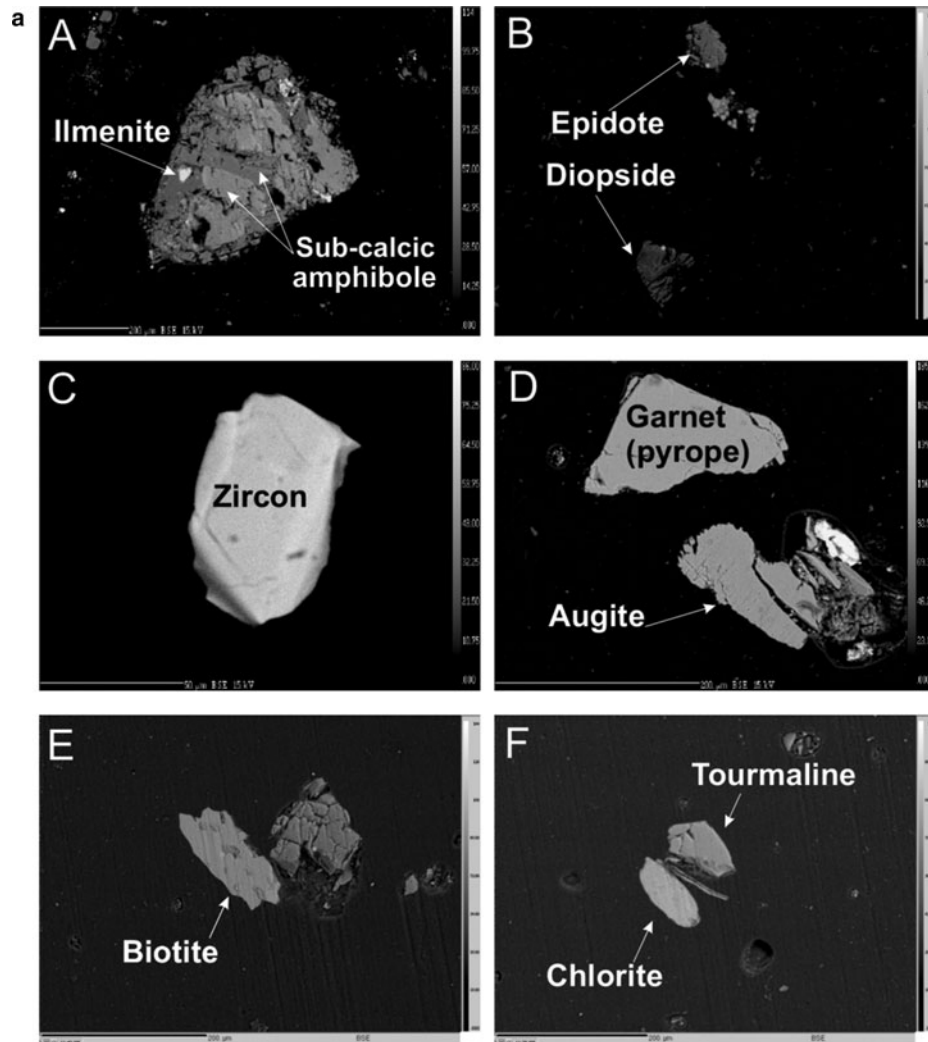
Fig. 3. **a.** Selected back-scattered electron images of metamorphic minerals observed at various depths. Green dots represent the positions of electron probe micro-analyser point analyses of respective grains. **A.** Fused texture of two different sub-calcic amphiboles, indicating the metamorphic nature of these minerals. **B.** Diopside of metamorphic affinity. **C.** Smooth grain boundaries of zircon, indicating a metamorphic origin. **D.** Subhedral grains of pyrope and augite with smooth and equilibrated grain boundaries, indicating a metamorphic origin. **E.** Detrital biotite grain. **F.** Tourmaline and chlorite. **b.** Selected back-scattered electron images of igneous minerals observed at various depths. Green dots represent the locations of spot analyses in the respective grains. **A.** Anhedral grain of pigeonite and calcic plagioclase. **B.** Orthopyroxene of igneous origin associated with plagioclase. **C.** Detrital grains of apatite, titanite and orthopyroxene. **D.** Phenocryst of augite coexisting with plagioclase. **E.** Dissociated orthopyroxene grain; the outer texture of the grain indicates the effects of hydrothermal activity. **F.** Anhedral altered grain of pigeonite.

Methods

The examined sediments represent the ~200–600 measured compensated depth (mcd) interval corresponding to the ~6–13 Ma period (Fig. 2; Tauxe *et al.* 2012. The dominant grain size lies within the field of coarse silt to fine silt; hence, whole samples were taken for chemical treatment (Biswas *et al.* 2020) and entire detritals > 53 μm were considered for heavy media separation. Grain sizes ~1 mm were studied as rock fragments separately, which were derived as IRD. The heavy mineral grains were separated via Bromoform and drained from the bottom of the flasks into funnels lined with WHATMAN #40 filter paper. The grains were thoroughly rinsed with distilled water and dried for 12 h. One extraction produced an average of ~0.3–0.5 g of heavy mineral grains, yielding ~100 grains on average. However, the population of heavy minerals varies throughout the depth. The entire separated portion of the heavy fraction was mounted on a glass slide. Approximately 60% of the total mounted grains were analysed. The mounted slides were analysed using
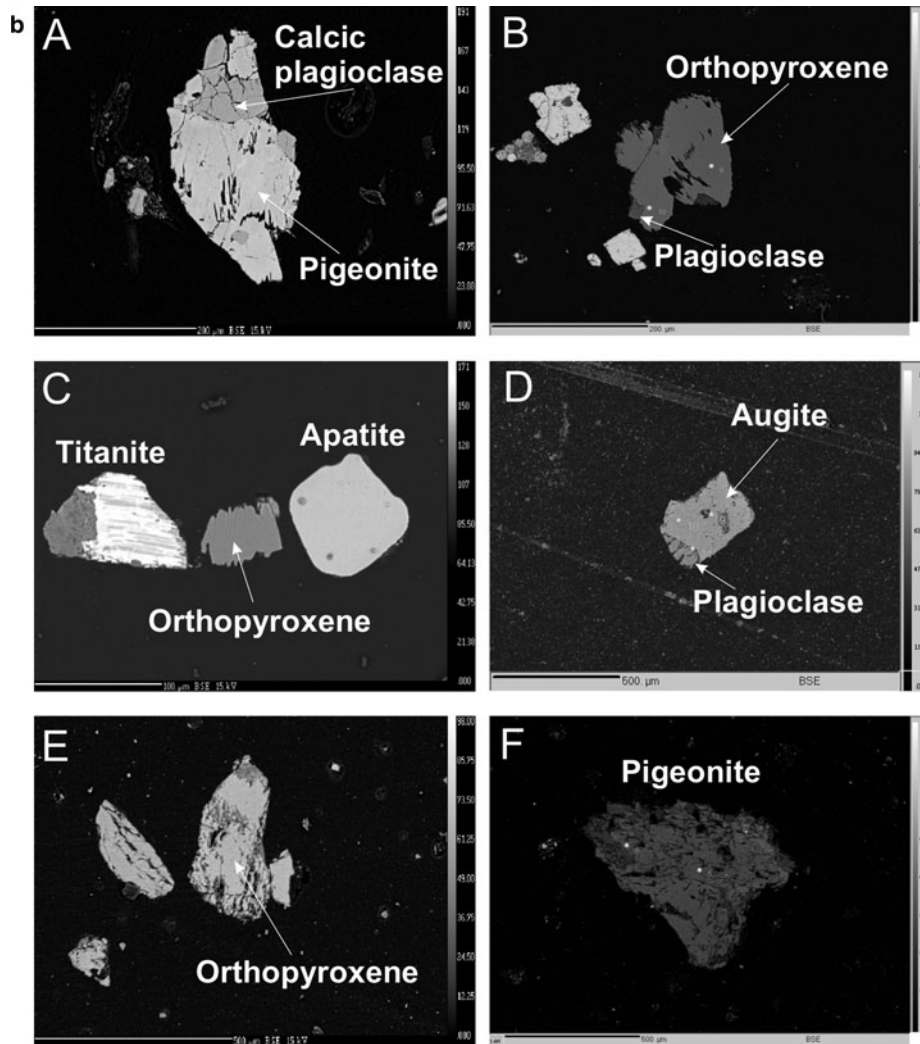
Fig. 3. (Continued)

energy-dispersive spectrometry (EDS) attached to a scanning electron microscope (SEM) and an electron probe micro-analyser (EPMA).

SEM-EDS analyses were carried out at the Department of Geology, University of Delhi, India, on a Zeiss SEM fitted with a Cambridge EDS and at the Department of Geology, Banaras Hindu University, Varanasi, India, on a Zeiss SEM fitted with a CAMECA EDAX EDS. The EPMA analyses were carried out at the Geological Survey of India, Faridabad, India, on a four-spectrometer CAMECA SX100 electron microprobe. The operating conditions for silicate analysis were 15 kV of high voltage and 10 nA beam current with a beam diameter of 1 µm or less. Natural mineral standards were used for calibrations. Calibrations for monazite were carried out at 20 kV and 20 nA (Pant *et al.* 2009). For monazite, Pb M_α was measured on an large pentaerythritol (LPET) crystal and the peak counting time was 240 s, with the

background measured on both sides. For better statistics and counting, sub-counting was done four times with the background measured each time for Pb. For uranium, measured using an LPET crystal, the U M_β line was used to avoid interference with the Th M_β line, with a peak counting time of 120 s and a background time of 60 s on both sides of the peak. The thorium M_α peak was also counted for 240 s and the background for 120 s on a pentaerythritol (PET) crystal. Rare Earth elements measured and the X-ray lines used included La (L_α), Ce (L_α), Nd (L_α), Pr (L_β), Sm (L_α), Ho (L_β), Dy (L_α) and Gd (L_β). Positions for background measurements were derived using the simulation software *Virtual WDS* (wavelength-dispersive spectrometry; Reed & Buckley 1996). Counting time at the peak varied from 40 to 60 s for these elements. The Y L_α line was used for yttrium, and it was counted for 240 s on peak and 120 s for background on both sides. The interferences of Y L_λ on
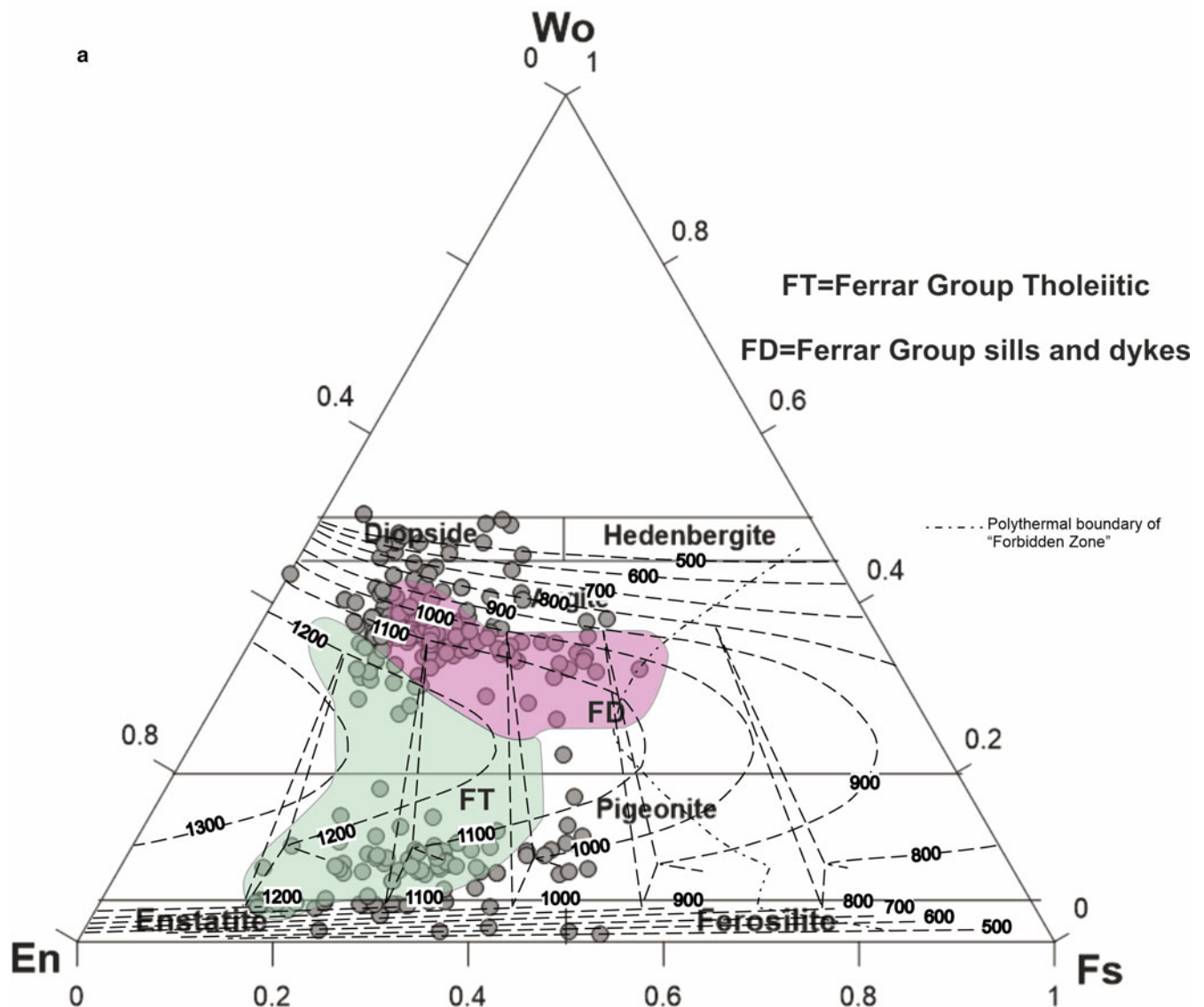
Fig. 4. Classification diagrams of pyroxene **a.** after Morimoto *et al.* (1988), showing plots of detrital pyroxene of site U1359. The abundance of augite and pigeonite is clearly visible. Isotherms are plotted to explain the stability temperature field for the formation of pigeonites and augite ranging from 800°C to 1200°C (Lindsley & Andersen 1983). **b.** Plot of Al_2O_3 *vs* FeO + MgO for distinguishing between igneous and metamorphic orthopyroxenes from the heavy fraction of U1359 (fields after Rietmeijer *et al.* 1983). Opx = orthopyroxene.

Pb M_α and Th M_β on Pb M_α were corrected after measuring the interfering lines during calibration and thereafter applying the overlap correction. The standards used for Pb, U and Th were crocite, U-glass and Th-glass. Synthetic silica-aluminium glass containing 4% rare Earth elements were used as standards for La, Ce, Nd, Pr, Sm, Ho, Dy and Gd. Phosphorus was calibrated with apatite. For Y, yttrium aluminium garnet was used. Al and Fe were calibrated using corundum and hematite, whereas, for silica content, orthoclase was used. Further details of the analytical procedure are given in Pant *et al.* (2009).

Results

Mineral chemistry of the heavy minerals

Pyroxene dominates the total heavy mineral population followed by amphiboles, garnet, biotite magnetite and other phases. In the following sections, we present the mineral-wise description of this chemistry, which is significant for inferring the lithology of the provenance regions and subsequent igneous and metamorphic subglacial terrain interpretations. Based on the textures and chemical composition of the heavy minerals observed from the backscattered electron (BSE) image
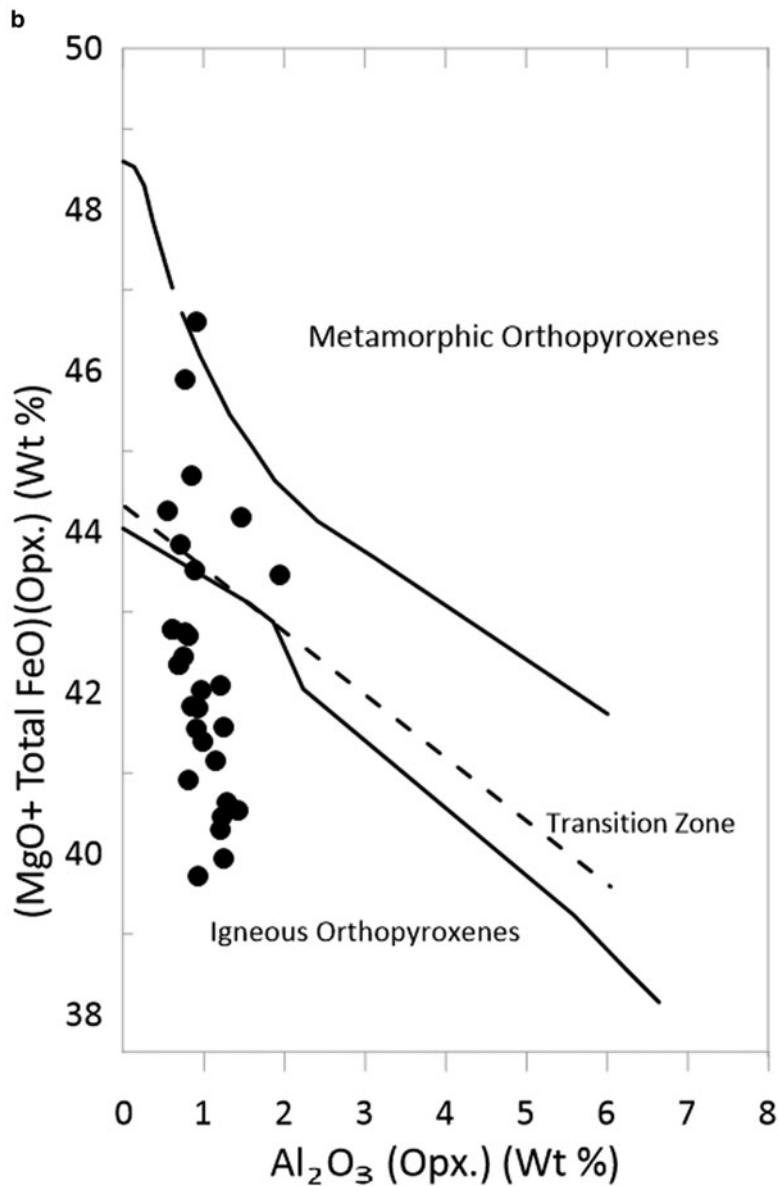
b

Figure: Plot of (MgO+ Total FeO)(Opx.) (Wt %) on the y-axis (from 38 to 50) versus Al_2O_3 (Opx.) (Wt %) on the x-axis (from 0 to 8), showing fields labelled "Metamorphic Orthopyroxenes", "Transition Zone", and "Igneous Orthopyroxenes" with scattered data points.

Fig. 4. (Continued)

and microprobe point analysis, two affinities of igneous and metamorphic origin can be easily distinguished. Figure 3a shows the BSE images of major metamorphic minerals observed in the sediments of site U1359, such as pyroxene, ilmenite, almandine, pyrope, spessartine, biotite, amphibole, zircon, *etc.* Figure 3b shows the igneous affinity minerals, such as pigeonite, calcic plagioclase, apatite, titanite and pyroxenes. Overall, the populations of zircon and monazite were rare, as the generalized sub-ice Wilkes Land terrain is considered to be an ultramafic/mafic igneous terrain (FLIP).

Pyroxene

The pyroxene classification of Morimoto *et al.* (1988) is used to differentiate pyroxene based on its chemical composition. All pyroxene analyses conform to the Ca-Mg-Fe or Quad chemical group (Morimoto *et al.* 1988) as shown in Fig. 4a. Pyroxenes with Ca < 5% are considered orthopyroxene in this work as the grains are too fine to resolve optically as orthorhombic or monoclinic crystals.

Orthopyroxene ranges from $En_{46}Fs_{53}Wo_{01}$ at 200–203 mcd to $En_{83}Fs_{14}Wo_3$ observed at 322–327 mcd. Mg-rich
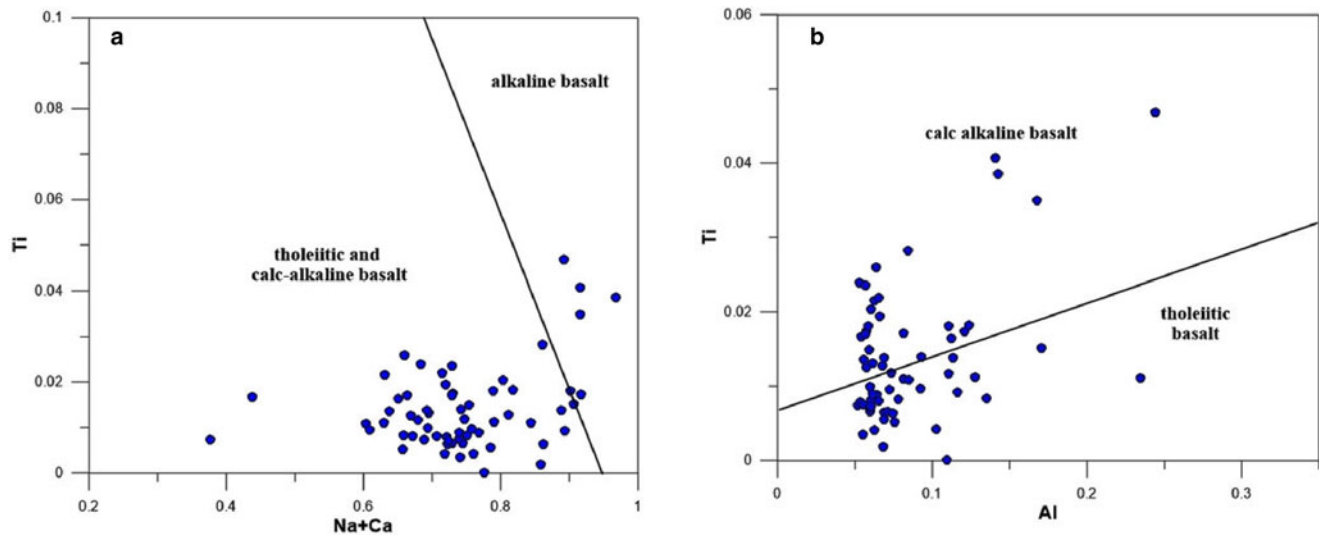
Fig. 5. Discrimination diagrams of Leterrier *et al.* (1982) for clinopyroxenes present in the heavy media of sediments of site U1359: **a.** Ti *vs* Na + Ca (in atoms per formula unit); **b.** Ti *vs* Al (in atoms per formula unit).

orthopyroxenes (enstatite) are present throughout the depth up to ~508 mcd (Table S1). No orthopyroxene grains were identified below this depth. Fe-rich orthopyroxene is reported from ~200 and ~280 mcd. Figure 4b shows that the orthopyroxenes present are of predominantly igneous affinities, but certain grains align towards the metamorphic field based on their FeO + MgO and Al_2O_3 contents (Rietmeijer *et al.* 1983), corroborated texturally by the annealed nature of metamorphic grains (Fig. 3a, panel B). Orthopyroxene of igneous origin is shown in Fig. 3b (panel E), where it is associated with plagioclase. The grain is subhedral and shows slight weathering at the outer boundaries, indicating chemical alteration. The transition-zone orthopyroxene can be of igneous as well as metamorphic origin (Rietmeijer *et al.* 1983).

Pigeonite, augite and diopside are major components and clinopyroxene is present throughout the investigated depth range. Augite dominates the heavy mineral assemblage followed by pigeonite and diopside. Pigeonite ranges in composition from $En_{77}Fs_{08}Wo_{15}$ to $En_{41}Fs_{42}Wo_{17}$ (Table S2). The MgO/MgO + FeO ratio varies from 0.34 to 0.92. Pigeonite is typically of igneous volcanic origin. It usually occurs as a phenocryst in mafic volcanic rocks. Since it is an unstable mineral at lower temperatures and it breaks down to orthopyroxene and augite, its presence suggests a shallow-level crystallization or volcanic activity associated with a relatively fast-ascending magma, resulting in the preservation of pigeonite phenocryst. The Fe/Mg ratio is controlled by the temperature of the magma: higher Mg values indicate a higher temperature (Robinson *et al.* 1977). The clinopyroxene classification diagram also shows the contours of the isotherms. None

of the clinopyroxenes fall in the forbidden zone and hence represent a population of stable clinopyroxenes. The isotherms suggest higher formation temperatures for the pigeonites and augites, ranging from 800°C to 1200°C (Lindsley & Andersen 1983). Compositionally, augite varies from $En_{57}Fs_{14}Wo_{29}$ to $En_{26}Fs_{32}Wo_{42}$. X_{MgO} ranges from 1.00 to 0.39 (Table S3), which is a significant variance, indicating that they might have evolved from different sources (e.g. magmas). Augites of Ca affinity are typically of igneous origin (basalt or andesite).

There is no distinct way to differentiate compositions of metamorphic augite from igneous augite, except based on their texture. We observe both types of augites in our samples. Diopside is also present as a major phase (Table S4), suggesting the possibility of ultramafic igneous rocks such as kimberlites or peridotites and/or contact-metamorphosed skarns developed from high-silica dolomites in the provenance.

We characterize the type of mafic source of pyroxenes based on the geochemical criteria defined by Leterrier *et al.* (1982). Geochemically, the clinopyroxene derived from intermediate to acidic rocks has an Al^{iv} content ranging from 0.03 to 0.05 atoms per formula unit on a six O basis (a.p.f.u.), while values of Al^{iv} content higher than 0.05 are found to belong to mafic volcanic rocks (Rodriguez-Gonzalez *et al.* 2012). Therefore, clinopyroxene with a Al^{iv} content higher than 0.05 is considered for geochemical discriminant diagrams. The results show that most of the samples indicate a tholeiitic basalt and calc-alkaline basalt as the prime source rocks (Fig. 5a,b). A few grains show affinity towards calc-alkaline basalt as well (Fig. 5b).
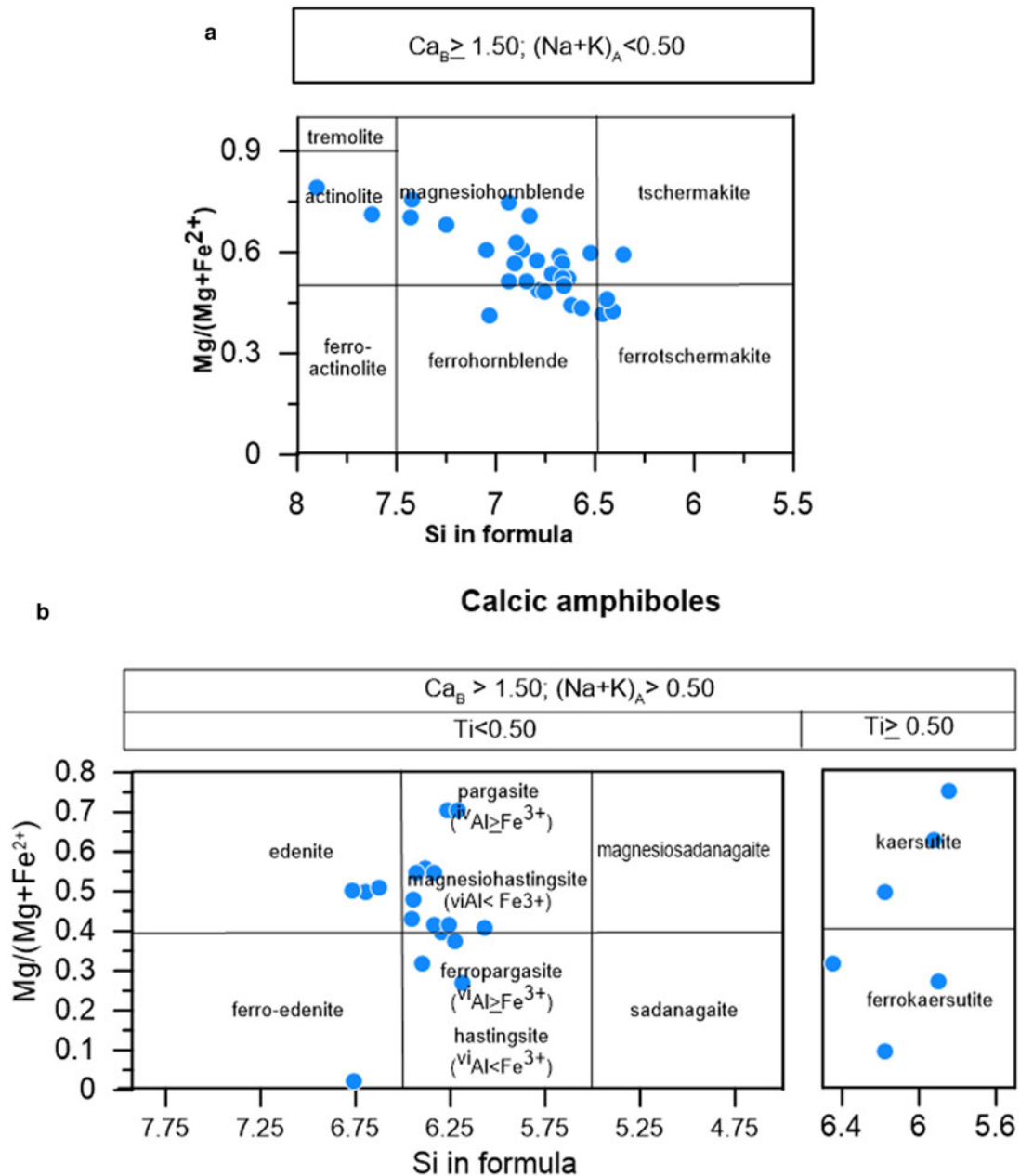
Fig. 6. Composition plots of calcic amphiboles from the sediments of site U1359 on the classification diagram devised by Leake *et al.* (1997). **a.** (Na + K)A ≥ 0.5, showing the dominance of actinolite and magnesio-hornblende. **b.** (Na + K)A < 0.5, showing the dominance of edenite and pargasite. **c.** Composition of calcic amphiboles from the sediments of site U1359 on the Al^{vi} *vs* Al^{iv} discrimination graph of Leake (1965).

Amphibole

The chemical composition of the analysed grains reveals the occurrence of chiefly four types of amphiboles: sub-calcic amphiboles, calcic amphiboles, sodic-calcic amphiboles and sodic amphiboles (classification based on Leake *et al.* 1997). Since lithium is not discernible from EPMA, magnesium-iron-manganese-lithium amphiboles (also termed sub-calcic amphiboles) were inferred by the very low value of calcium and sodium, calculated for site B, as compared to the other groups of amphiboles (Table S5).

Figure 6a shows the presence of actinolite, magnesio-hornblende, ferro-hornblende, tschermekite and ferro-tschermekite. In Fig. 6b, the grains are classified as edenite, pargasite, ferro-edenite, ferro-pargasite, kaersutite and ferro-kaersutite. Magnesio-hornblende, actinolite, edenite and pargasite are present as dominant phases, while
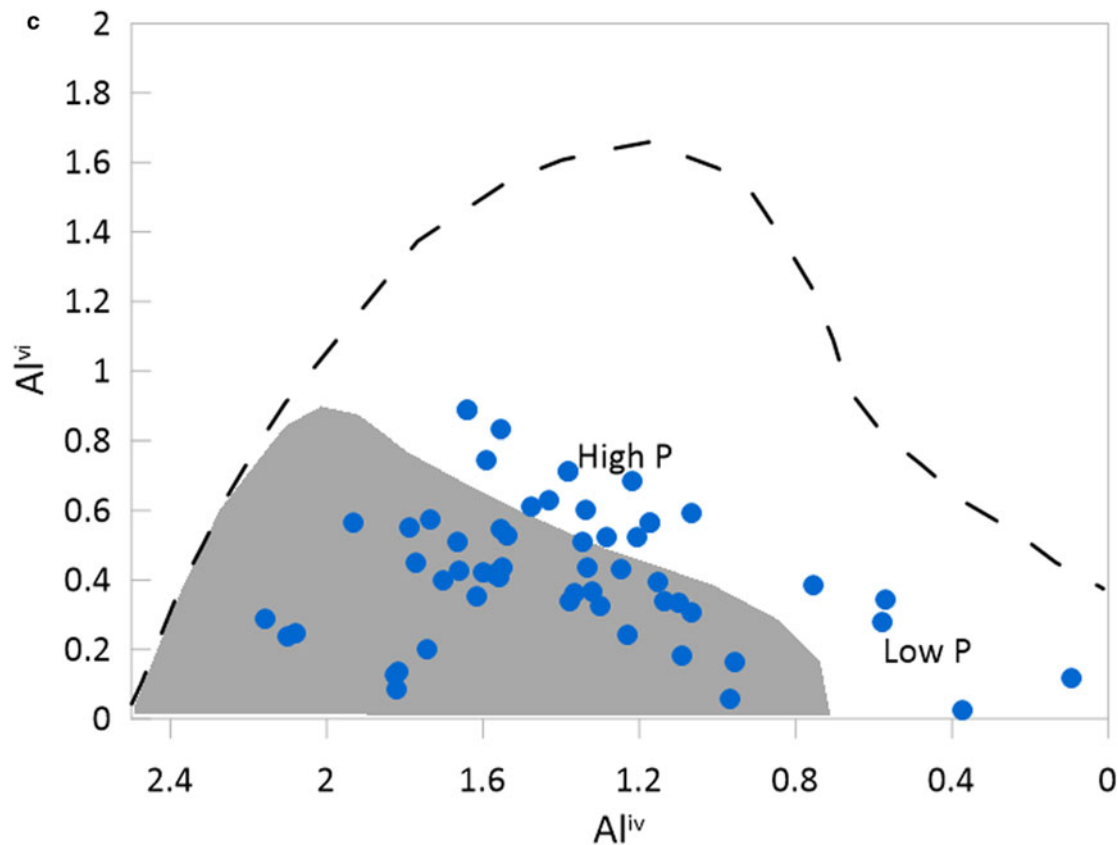
Fig. 6. (Continued)

ferro-hornblende, ferro-actinolite, tschermekite, ferro-tschermekite, ferro-edenite, ferro-pargasite, kaersutite and ferro-kaersutite are less abundant. Their representative analyses are given in Table S6. Actinolite and magnesio-hornblende with high Si a.p.f.u. values are related to metamorphic sources, while magnesio-hornblende with medium to low Si a.p.f.u. values and other calcic amphiboles such as ferro-hornblende and ferro-tschermakite belong to the igneous plutonic source (Rodriguez-Gonzalez *et al.* 2012).

The Al^{vi} and Al^{iv} values (in a.p.f.u.) of calcic amphiboles are used to chemically distinguish igneous and metamorphic amphiboles (Fig. 6c). The grey field in Fig. 6c indicates a plutonic igneous source and the white portion outlined by a dotted line indicates the field of metamorphic calcic amphiboles (Leake 1965, Rodriguez-Gonzalez *et al.* 2012).

Detrital calcic amphiboles of site U1359 cover almost all of the fields with variable abundances. There is almost an equal amount of igneous as well as metamorphic sourcing of amphiboles. Amphiboles of metamorphic affinity predominantly belong to a high-pressure metamorphic belt, but a few samples also have an affinity to the low-pressure metamorphosed belt (Fig. 6c). The presence of sodic-calcic and sodic

amphiboles indicates the possibility of the presence of blueschist facies rocks within a subglacial metamorphic terrain in the WSB region. However, this inference would require confirmation in the form of additional high-pressure minerals.

Garnet

The representative analyses of garnet are given in Table S7. Garnet is a characteristic mineral of metamorphic origin. However, it is also reported from acidic igneous rock (Deer *et al.* 1992). Chemically, garnet varies from $Alm_{80}Py_{15}Sps_3Grs_2$ to $Alm_{45}Py_{36}Sps_1Grs_{18}$. The classification of garnet is carried out on the trilinear plot of Fe-Mn-Mg-Ca formulated by Mange & Morton (2007) (Fig. 7a). The diagram classifies detrital garnet identified from sediments of site U1359 in five divisions and subdivisions based on their chemical characteristics. It also aids in describing the most probable source for the garnet.

Type A garnets typically have high Mg and low Ca. These garnets are generally considered to be derived from high-grade granulite facies metasedimentary sequences (Sabeen *et al.* 2002, Morton *et al.* 2004), but they can also be derived from intermediate silicic
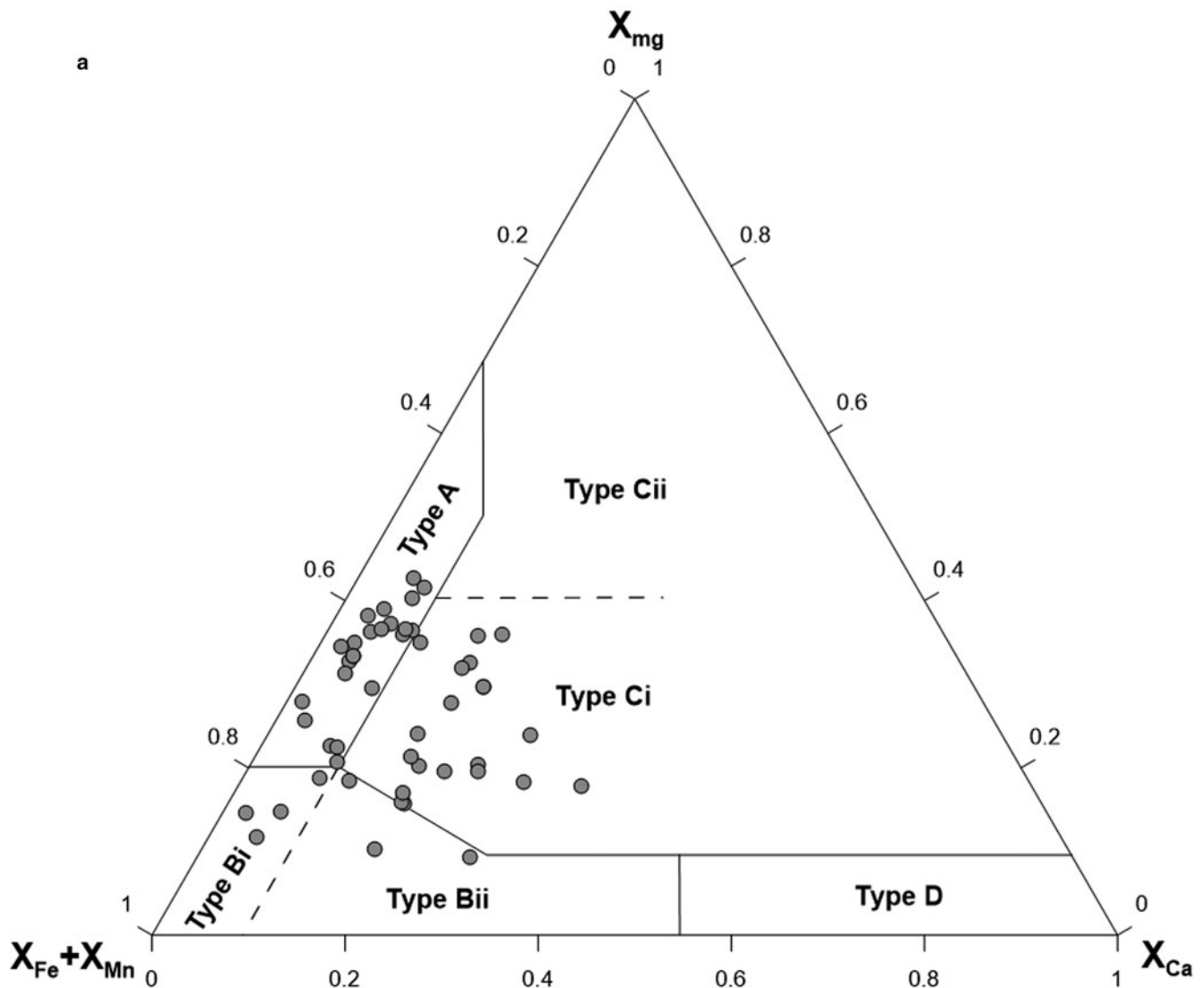
Fig. 7. Classification of garnet, biotite and feldspar. **a.** Subdivision of garnet in the Fe + MFn-Mg-Ca ternary plot devised by Mange & Morton (2007), showing the presence of type A, B and C classes of garnet in the detrital sediments of site U1359. **b.** Classification of biotite based on the Fe/(Fe + Mg) *vs* Al content. Grey circles represent biotite data from the present study while black circles represent the biotite data published in Pant *et al.* (2013). **c.** Ternary phase diagram of the feldspars obtained from Greenwood & Earnshaw (1998). Diamonds represent the feldspars present in the sediments of site U1359, which are associated with the pyroxenes and amphiboles.

igneous rock (Green & Ringwood 1968, Fitton 1972, Hamer & Moyes 1982). In the proximal Wilkes Land terrain, the most probable source for type A garnet is granulite facies metasedimentary rocks, as we also found metamorphic orthopyroxene, which is typical of granulite facies metamorphism.

Type B garnet has low Mg and variable Ca. These garnets are derived from amphibolite facies metasediments. Two subgroups are distinguished based on the X_{Ca}%: Bi, which has $X_{Ca} < 10$%, and Bii, which has $X_{Ca} > 10$%. The population within the Bi field is from either intermediate acidic rocks or low-grade metasedimentary rocks.

Type C garnets are rich in Mg and Fe. Two subclasses are distinguished here based on the X_{Mg} content: Ci has $X_{Mg} < 40$% and Cii has $X_{Mg} > 40$%. Almost 50% of the garnet grains fall in the field of Ci and are interpreted to be derived from a metabasic sequence.

Biotite

Representative biotite analyses are listed in Table S8, and the structural formula is calculated based on 11 oxygen atoms. High Ti biotite was reported previously from the Plio-Pleistocene sediments of the same core (Pant *et al.*
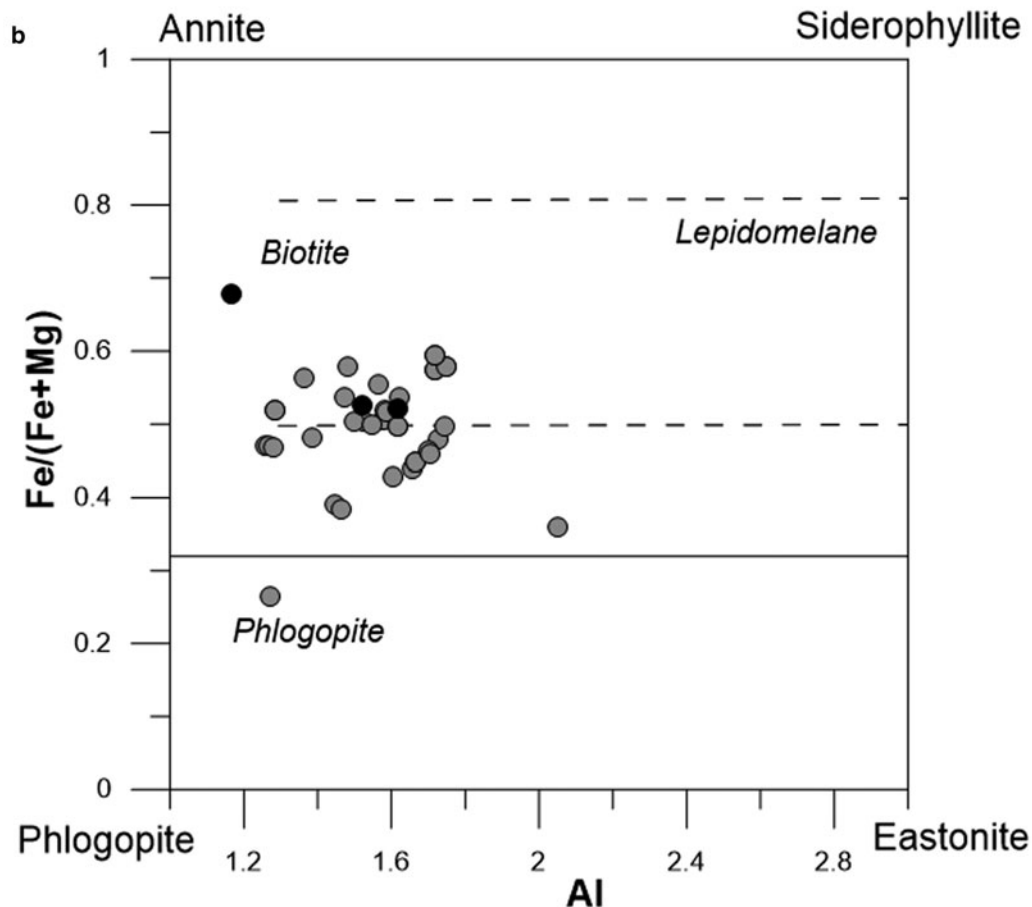
Fig. 7. (Continued)

2013); however, Miocene sediments show a predominance of low to moderate Ti and Fe contents (Fig. 7b) and have higher MgO (TiO$_2$ < 1.5%; MgO ~11–13%) in biotite. The chemical composition of biotite without associated assemblages is insignificant for distinguishing the mode of genesis. However, a moderate to low Ti content is suggestive of medium-grade metamorphic and/or acidic-intermediate magmatic sourcing.

Feldspars

The feldspars found in the heavy mineral population of the sediments of site U1359 are associated with pyroxenes and amphiboles. Their structural formula is calculated based on eight oxygen atom and the representative analyses are given in Table S9. A classification of feldspar was also carried out (Fig. 7c). Plagioclases are common feldspar grains in the analysed fractions.

There are two chemical variants present, with one being high in calcium (An > 50) and the other of low-intermediate composition (An < 50; Fig. 7c); both show considerable variation. High-calcium plagioclase

also belongs to two categories, with one representing a narrow range (An$_{50–70}$) and the other of bytownite (An$_{70–90}$) composition. The low-intermediate calcium plagioclase (An$_{0–50}$) represents at least two metamorphic sources, one rich in albite (X$_{Ab}$ > 90) and the other with a range of values from An$_{20}$ to An$_{40}$. The narrow range of anorthite content of high Ca represents a basaltic magmatic source. The ternary plot of the feldspar classification shows the presence of K-feldspar in the sediments. Its presence is common in felsic volcanic and plutonic rocks. However, it has also been reported from ultrapotassic mafic, high-temperature contact metamorphic rocks and hydrothermally altered rocks.

Ilmenite

The representative ilmenite analyses are reported in Table S10. Chemically, Basu & Molinaroli (1991) found that ilmenite grains with TiO$_2$ contents between 50 and 60 wt.% are more prevalent in metamorphic rocks, but they also occur in igneous rocks ranging between 40 and 50 wt.%.
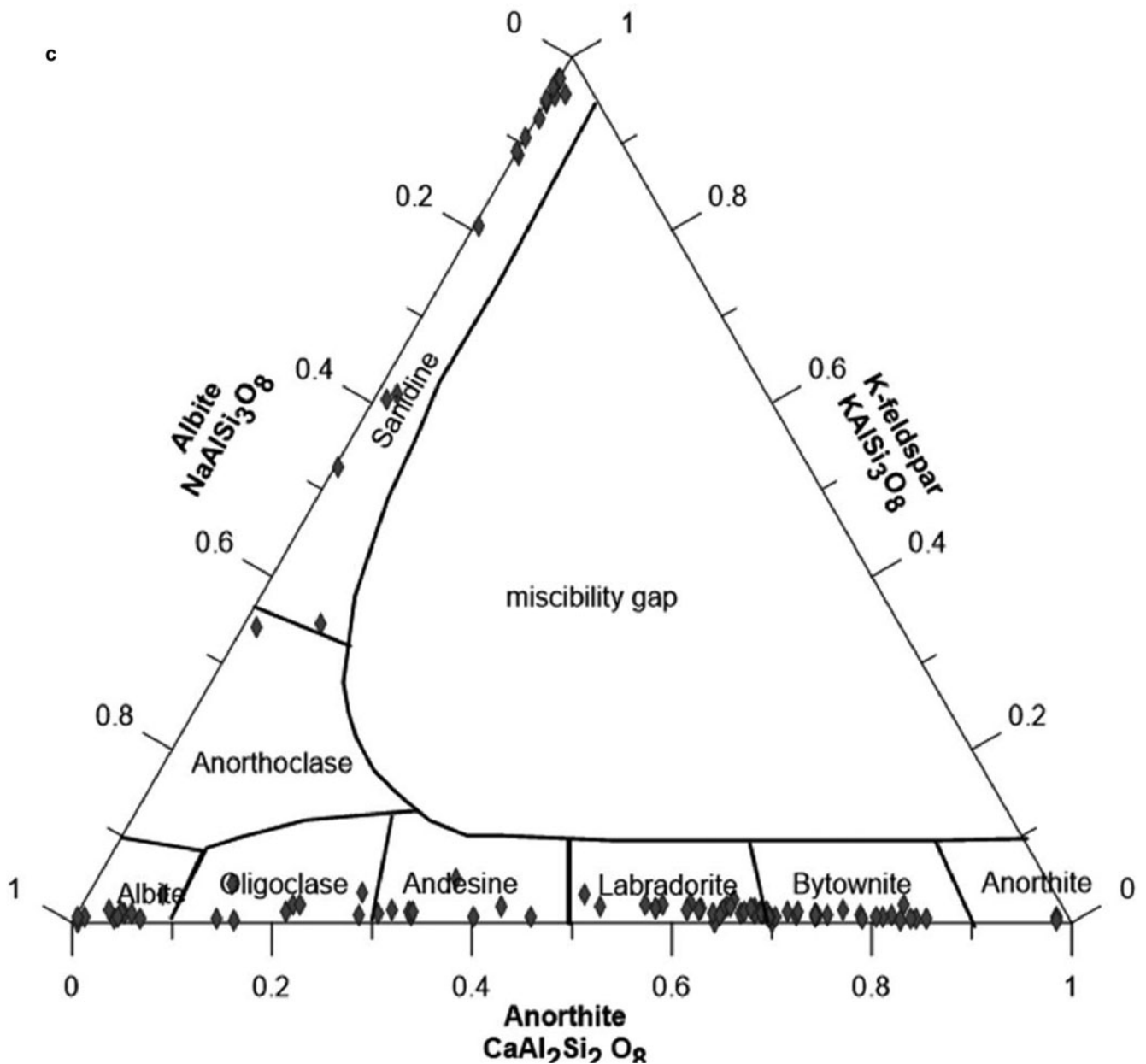
Fig. 7. (Continued)

Schneiderman (1995) noted that ilmenite from metamorphic sources is richer in TiO_2 than ilmenite in igneous rocks. Here, we found both types of ilmenites, with a predominance of ilmenite with TiO_2 ranging from 40% to 50%, which is taken here as being indicative of an igneous origin; however, 17 grains out of 40 show values that suggest derivation from metamorphic rocks instead.

Epidote, sphene, scapolite, cordierite, Ba-silicates, magnetites, apatite, rutile, Fe-hydroxides, sulphides, titanomagnetite, zircon, *etc.*, are the other heavy minerals that were observed in trace amounts. A wide range of chemically distinguishable mineral species indicate the presence of rather a complex terrain comprising a low-grade as well as a high-grade metamorphic provenance and a mafic igneous source.

Mineral chemistry of the rock fragments

Detrital rock fragments provide the most valuable tool for investigating potential source rocks. Rock fragments are the detritals derived from certain lithologies as IRD and consist of more than one texturally constrained coexisting phase (Fig. 8a, left inset). These facilitate the
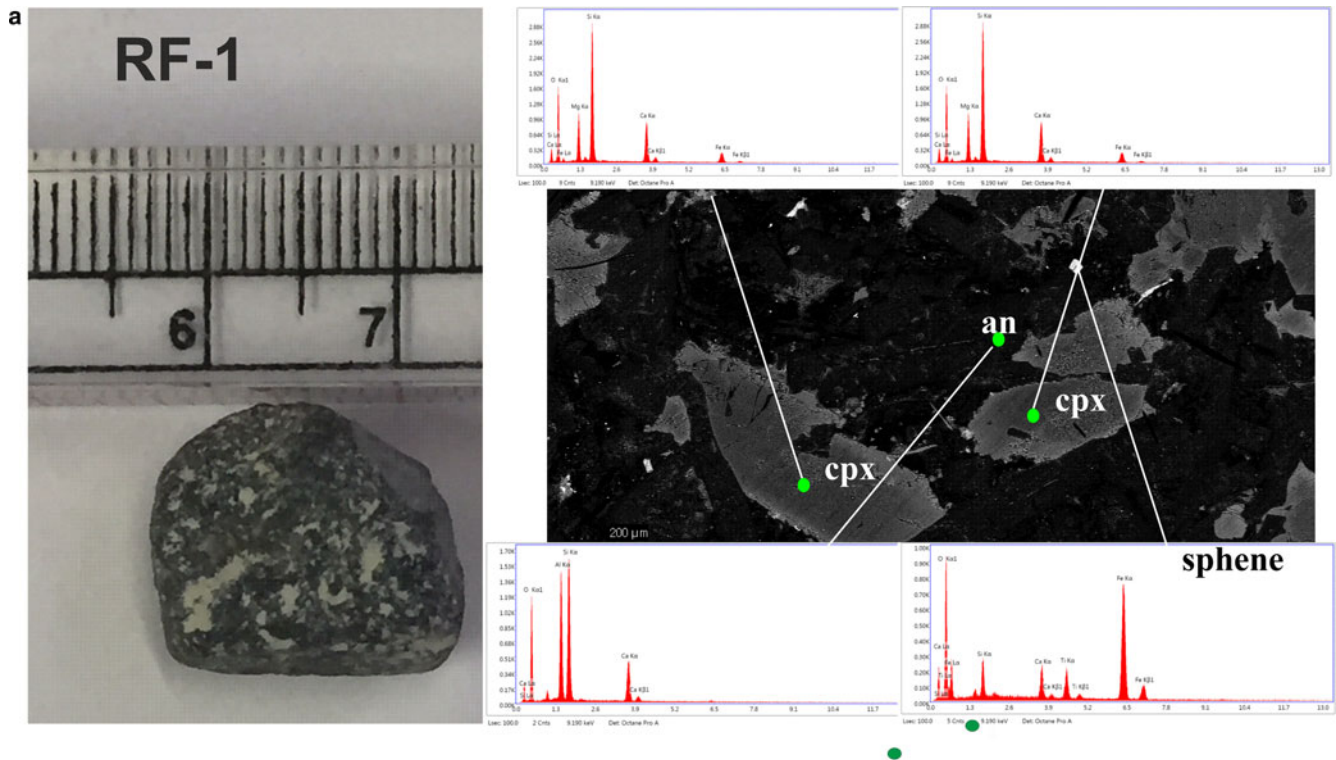
Fig. 8. Various selected rock fragments. **a.** Representative of rock fragments collected from various depths of site U1359 in the left inlet and back-scattered electron image of the igneous-origin rock fragment 1 (RF-1) with clinopyroxene (cpx) and anorthite (an) identified as major phases and sphene present as an accessory phase. **b.** Back-scattered electron image of RF-2: muscovite-biotite schist (green dot represents the location of spot analyses carried out by electron probe micro-analyser). The presence of schistosity confirms its metamorphic origin. **c.** Back-scattered electron image of RF-3: garnet biotite schist represented by a porphyroblast of garnet with inclusions of biotite and quartz.

interpretation of the genesis of the rocks and the tectonic setting of the provenance region as they preserve coexisting phases and textural features. In this study, we focused on three different rock types identified based on the texture and mineral composition of the associated phases: basalt fragment, garnet biotite schist and two-mica schist (Fig. 8). One representative rock fragment is of igneous origin, while the other two rock fragments are metamorphic in origin and are used here to further constrain the metamorphic conditions of the source rocks

Basalt/dolerite (rock fragment 1)

Rock fragment 1 (RF-1) is retrieved from 218.9 mcd (Fig. 8a), and the presence of a hypidiomorphic equigranular texture denotes it to be igneous in origin. Phenocrysts of clinopyroxene and calcic plagioclase are present as the major constituents and show a subophitic intergranular texture (Fig. 8a). EDS analyses of RF-1 classify clinopyroxene as augite (CaO ~25%, FeO and MgO ~12–13%), while plagioclase is anorthitic (CaO ~22%). Sphene is identified as an accessory phase.

The analyses reaffirm the presence of igneous-origin augite in these sediments.

Two-mica schist (rock fragment 2)

This rock fragment is recovered from the sediment depths of 230–233 mcd and represents a fine-grained schistose metamorphic rock with an assemblage of muscovite + biotite + quartz + ilmenite + monazite. Coexisting muscovite and biotite define the fine-grained schistosity (Fig. 8b). Compositionally, muscovite is present as the dominant phase, indicating the low-grade metamorphism of the pelitic source.

Representative analyses of the two-mica schist are given in Table S11. The a.p.f.u. values in the table are based on 11 oxygen atoms for biotite and muscovite and 5 oxygen atoms for ilmenite. The $X_{Mg}/(X_{Fe} + X_{Mg})$ values of biotite are 0.51–0.57, which signifies enrichment of Mg in biotite, and the Ti value ranges from 0.17 to 0.35 a.p.f.u., indicating a low-grade metamorphic terrain of the rock fragment. Ilmenite has Ti ~1.8 a.p.f.u and Fe ~1.2 a.p.f.u. Monazite is found to be associated with the two-mica schist (shown in Fig. 8b), and this is discussed in detail separately.
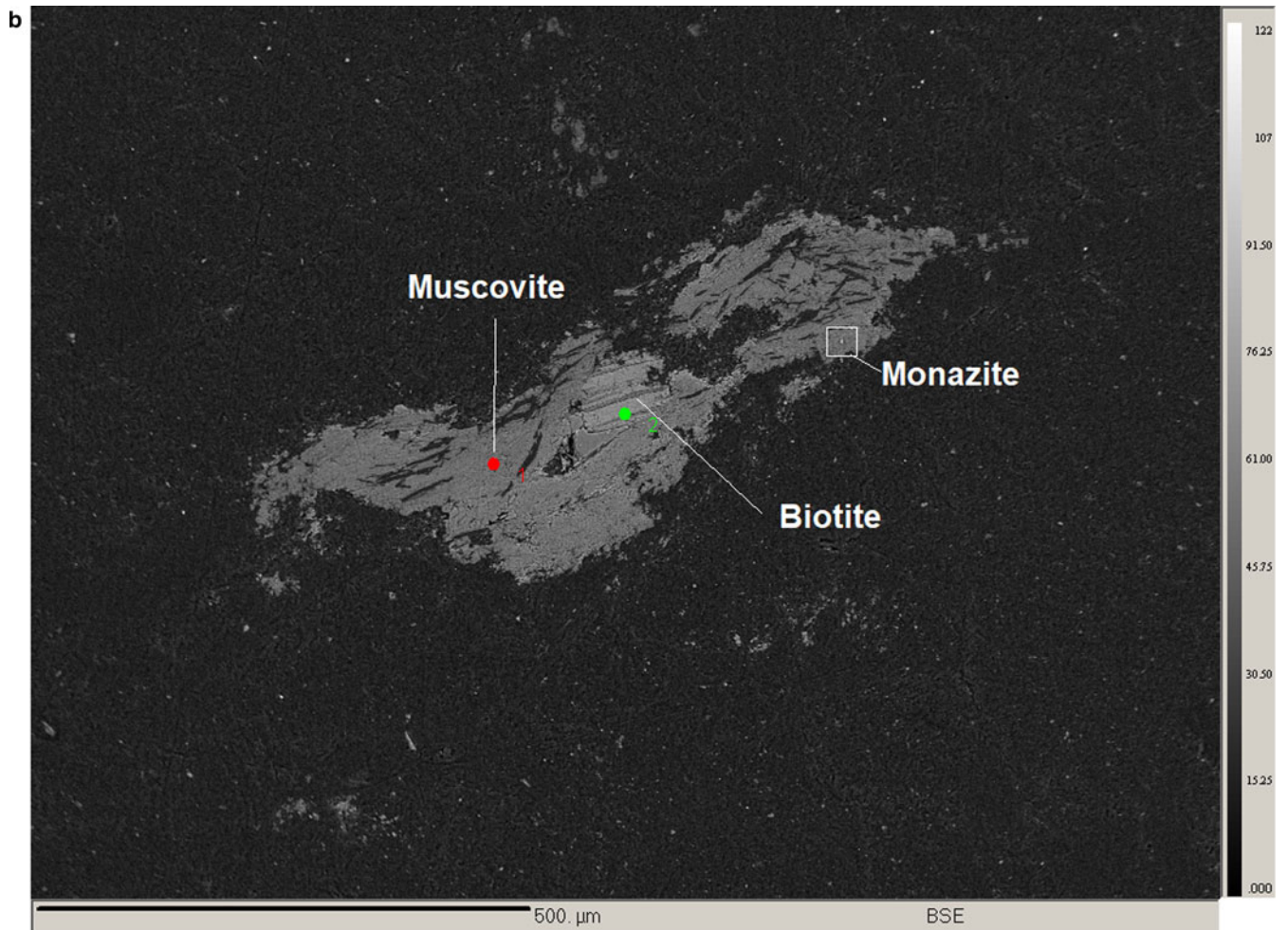
Fig. 8. (Continued)

Garnet biotite schist (*rock fragment 3*)

Porphyroblast of subhedral garnet associated with biotite and quartz is the third rock fragment we investigated to deduce metamorphic conditions. This rock fragment is recovered from the sediments in the depth range ~227–230 mcd.

Based on the observed features and mineral composition, the possible mineral assemblage for the garnet biotite schist is garnet + biotite + quartz. The typical metapelitic assemblage and the presence of internal schistosity in the porphyroblast of garnet attest to its metamorphic origin (Fig. 8c). The internal schistosity is defined by biotite and quartz. The size of the porphyroblast is ~400 μm. Garnet is subhedral with a smooth grain boundary, indicating the absence of any significant alteration. Garnet may have developed from the consumption of biotite and quartz during a possible second stage of metamorphism.

The representative mineral chemistry of garnet and biotite is given in Table S11. Garnet is compositionally homogeneous and almandine-spessartine rich with X_{Fe} ~0.57, X_{Mg} ~0.14, X_{Mn} ~0.23 and X_{Ca} ~0.04. The X_{Mg} of biotite is ~0.55 and Ti is 0.38 a.p.f.u., which are comparable to the values of biotite obtained from the two-mica schist. This indicates a similar genesis of the biotite of both rock types. The ~23% spessartine content also suggests that the garnet is of low-grade metamorphic origin.

Geothermometry

The mineral assemblages and mineral compositions of any type of rock are sensitive to the pressure and temperature conditions of formation if events subsequent to mineral equilibration have not significantly modified the original composition of these minerals. Hence, minerals in equilibrium can be calibrated for the estimation of the pressure and temperature conditions at which a geological material experienced a major event such as metamorphism. Considering Wilkes Land as the dominant provenance for the detritals of site U1359, there is a
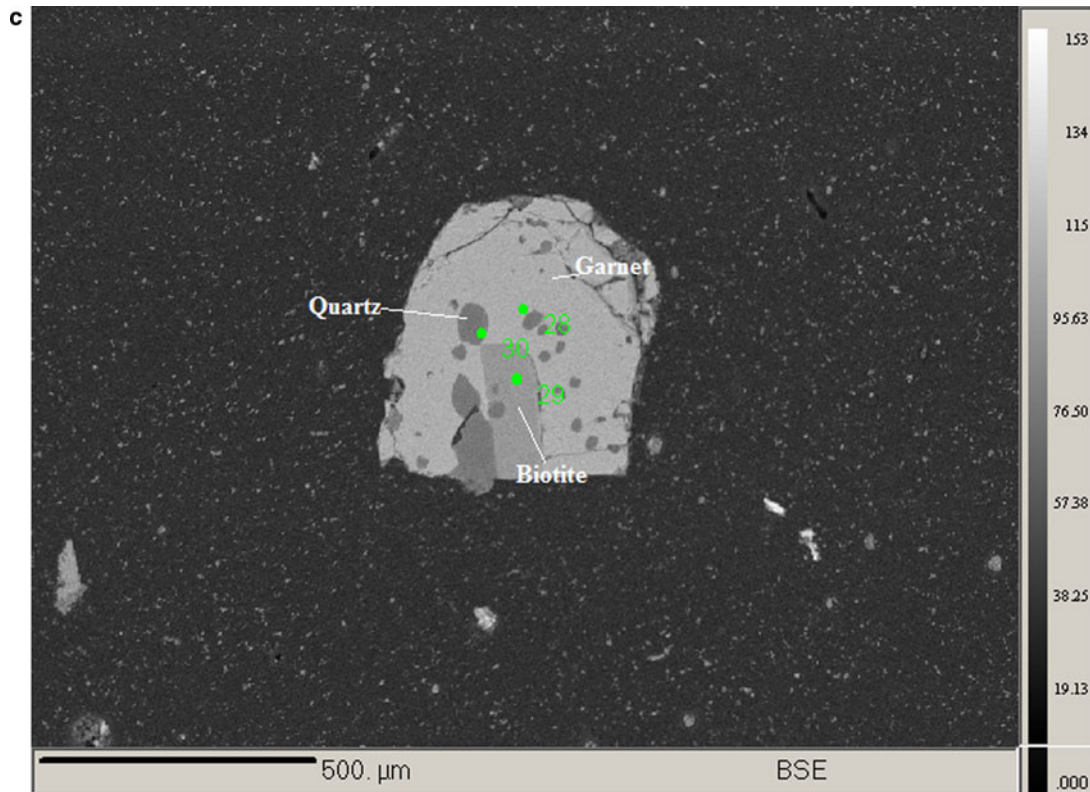
Fig. 8. (Continued)

possibility of the associated minerals of rock fragments being represented in thermodynamic equilibrium and hence being used to decipher the limiting metamorphic conditions existing in the provenance. For garnet-biotite schist rock fragments, the garnet-biotite formulations of Ferry & Spear (1978), Dasgupta *et al.* (1991) and Bhattacharya *et al.* (1992) are used. The estimated temperature is $\sim587 \pm 17°C$ at 7 kbar pressure, which indicates amphibolite facies metamorphic conditions.

Monazite geochronology

Site U1359 is the easternmost site drilled during IODP Expedition 318 on the continental rise. The chances of getting any geochronological signatures are reduced significantly due to its remoteness from the provenance. Moreover, the sub-ice terrain in Wilkes Land is dominantly an igneous province (Cook *et al.* 2013), which further diminishes the chances of getting any radioactive minerals as detritals. Despite these limitations, a monazite grain was found to be associated with the muscovite-biotite schist rock fragment. The grain is subhedral with a maximum dimension of $\sim40 \mu m$. The monazite is Ce rich with values ranging from 0.406 to 0.441 a.p.f.u. Th varies from 0.050 to 0.089 a.p.f.u. (all a.p.f.u. values are on a four oxygen atom basis), while P ranges from 0.883 to 0.937 a.p.f.u.

The Ca value ranges from 0.055 to 0.080 a.p.f.u., indicating the presence of solid solutions of brabantite and huttonite (Table S13). For individual spot ages, the formulation of Montel *et al.* (1996) was followed, whereas the age probability plots and unmixing of ages were obtained using the software *Isoplot* 3.00 (v.3.71.09.06.19nx; Ludwig 2003). Uncertainties in individual analyses in the data table and weighted mean ages are quoted at the 95% confidence level (2σ). The -distribution of age points is shown in Fig. 9a. The monazite provides a well-constrained age of 799 ± 13 Ma (Fig. 9b). The weighted average indicates 799 ± 25 Ma (Fig. 9c), whereas the chemical Th-U-total Pb isochron method (CHIME) age extracted from the monazite grain indicates an isochron age of 810 ± 20 Ma (Fig. 9d), confirming an event at ~800 Ma.

Discussion

Igneous and metamorphic origins of detritals are inferred based on the textures and chemical composition of the heavy mineral assemblage. Our classification of pyroxene shows the presence of orthopyroxene, pigeonite, augite and diopside. Further classification enables us to differentiate between metamorphic orthopyroxene and igneous orthopyroxene. Considering that clinopyroxene
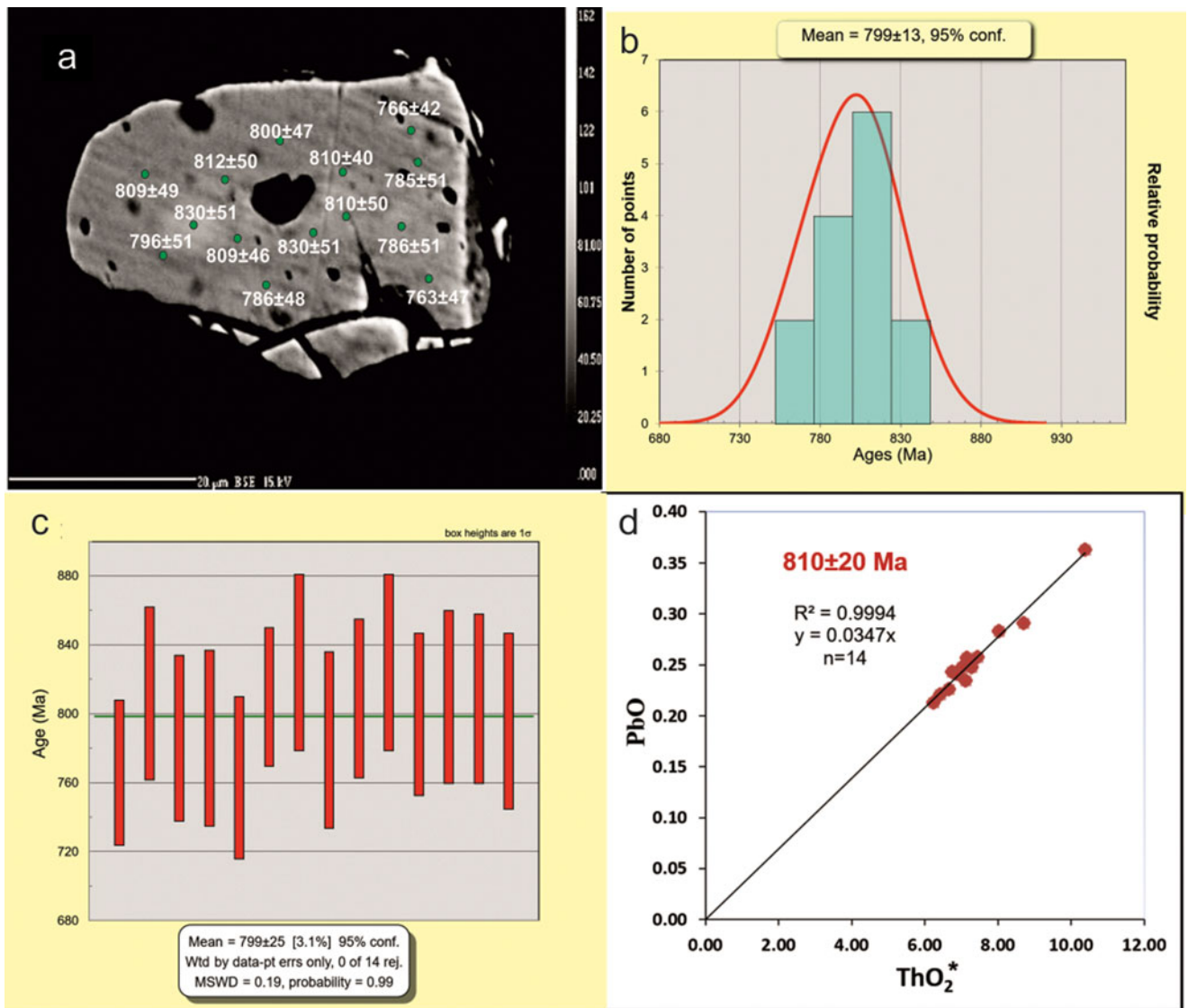
Fig. 9. a. Back-scattered electron image of monazite present in rock fragment 2 extracted from heavy mineral fractions at of depth 230–233 measured compensated depth marked with ages. **b,** Frequency diagram and weighted average of the age obtained from monazite. **c.** Weighted average indicates 799 ± 25 Ma. **d.** CHIME age extracted from the monazite grain, indicating an isochron age of 810 ± 20 Ma. CHIME = chemical Th-U-total Pb isochron method; MSWD = mean square of weighted deviation.

with $Al^{iv} > 1.5$ belongs to igneous sources, the analysis was used to infer the geochemical behaviour of the source basalt. The results show that most of the samples indicate a tholeiitic to calc-alkaline basalt as a prime source rock (Fig. 5a). Four different species of amphiboles present in the sediments are sub-calcic amphiboles or calcic amphiboles (Fig. 6a,b). The metamorphic and igneous calcic amphiboles are interpreted based on the discrimination graph in Fig. 6c. The calcic amphiboles and biotite of metamorphic affinity show characteristics of both high-grade as well as low-grade rocks, indicating the presence of both types of metamorphic belt in the sediment provenance region (Figs 6c & 7b). The classification of garnet defined by Mange & Morton

(2007) shows the presence of garnet belonging to granulite facies as well as amphibolite facies of metasediments (Fig. 7a). Minor sourcing from metabasic and ultramafic rocks is also indicated from the classification (Fig. 7a). The compositional variation of garnet corroborates our interpretation of two contrasting grades of metamorphism in the provenance region.

Two-mica schist (230–233 mcd) and garnet-biotite schist (227–230 mcd) are two different rock fragments that were studied to deduce the metamorphic conditions. Both of the rock fragments are metamorphic in origin, with the mineral assemblage for RF-2 (Fig. 8b) given as muscovite + biotite + quartz + ilmenite + monazite and that for RF-3 given as garnet + biotite + quartz
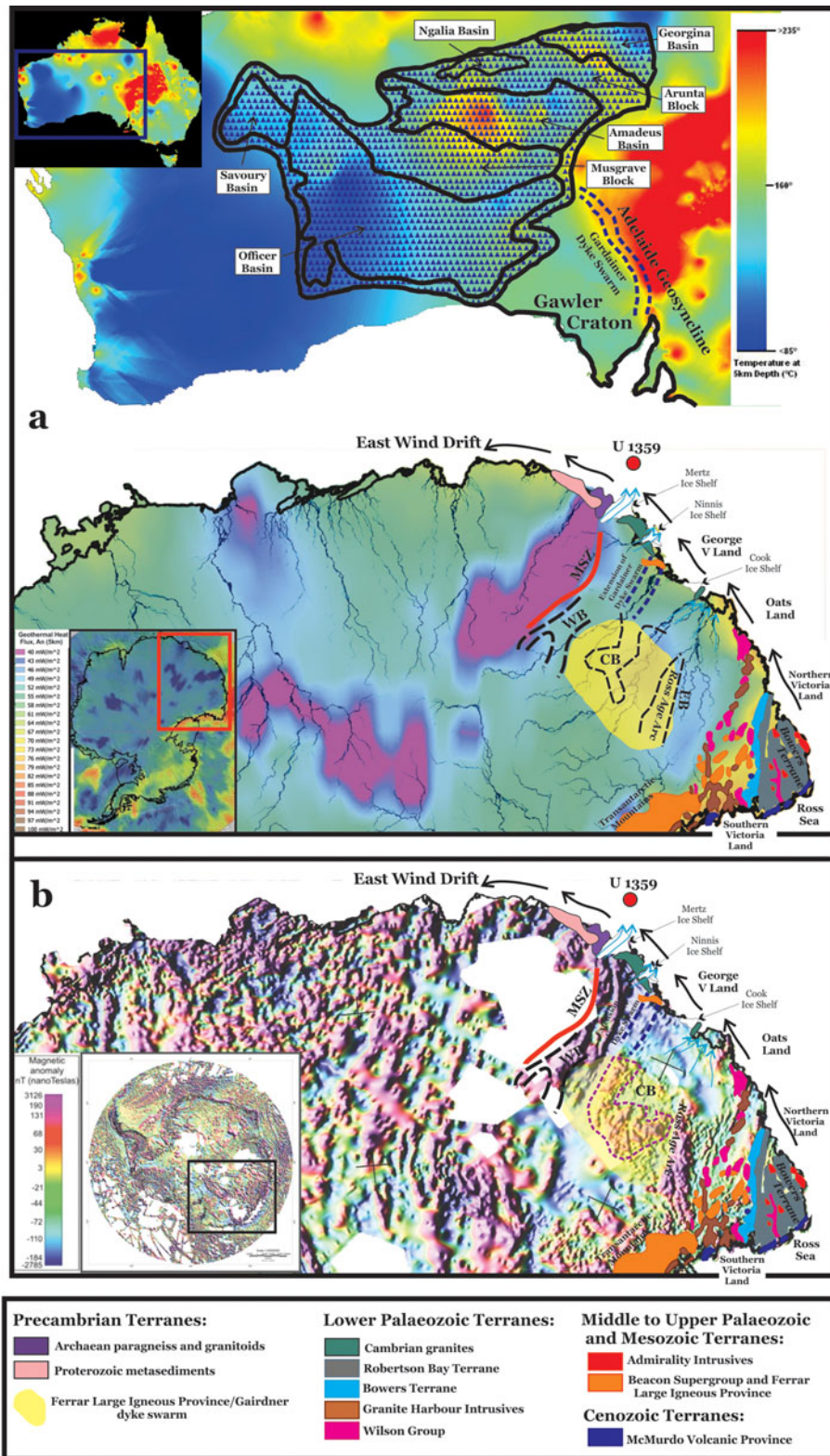
Fig. 10. Reconstructed map of geology and linkage of Australia and East Antarctica. **a.** The base map of Australia is from Gerner *et al.* (2010) and that of East Antarctica is from An *et al.* (2015), made using *Quantarctica* (Matsuoka *et al.* 2021). The Centralian Superbasin and its constituent basins in South Australia are inferred from Walter *et al.* (1995). Geologies of Adélie Land and North Victoria Land are as reported by Ménot *et al.* (2007) and Weaver *et al.* (1984), respectively. Locations of subglacial Eastern Basin (EB), Central Basin (CB) and Western Basin (WB) are from Ferraccioli *et al.* (2009). The probable area of extension of the Gairdner Dyke Swarm is shown by blue dashed lines in the interior of the Wilkes Subglacial Basin. **b.** Known geology of the study area overlaid on the ADMAP-2 aeromagnetic anomaly map (modified from Cook *et al.* 2013, Aitken *et al.* 2014, Golynsky *et al.* 2018). MSZ = Mertz Shear Zone.

(Fig. 8c). The presence of two-mica schist indicates low- to medium-grade metamorphic conditions. Temperature and pressure deduced as limited conditions agree with the inferred granulite facies and greenschist to amphibolite facies of metamorphism, respectively. Signatures of greenschist to a granulite grade of metamorphism are evident from the mineral chemistry as well as pressure-temperature estimations, indicating the presence of a mobile belt in the source domains. Chemical dating of monazite provides a well-constrained age of 799 ± 13 Ma (Fig. 9) from the low-grade assemblage, evincing the presence of a low-grade metamorphic event during Neoproterozoic (Tonian) times.

The geology of the Wilkes Land sector is predominantly inferred through 1) unconstrained projections of its Australian counterpart (Boger 2011), 2) geophysical signatures suggesting the Proterozoic basement provinces accreted during supercontinental assemblies (e.g. Golynsky *et al.* 2018) and 3) geochronological dating of detrital zircons and monazites recovered from the offshore sediments and exposed sedimentary rocks (e.g. Pierce *et al.* 2017, Daczko *et al.* 2018).

The WSB is almost 600 km wide along the Coats Land coast and is > 1400 km long (Bedmap2; Fretwell *et al.* 2013). It includes a variety of sub-basins identified from radar data and defined as the Eastern Basin, Central Basin and Western Basin (Ferraccioli *et al.* 2009) separated by highlands (Frederick *et al.* 2016; shown in Fig. 10). The main source of sediment supply from the WSB is predominantly along Mertz Glacier through ice streams, which is the close to the drill site (Rignot *et al.* 2011, Pant *et al.* 2013). Other more distal ice streams capable of delivering sediments to the IODP site include Ninnis Glacier, which follows the Western Basin, and the underlying Central Basin delivers its sediment to the western and eastern Cook ice streams (Ferraccioli *et al.* 2009, Frederick *et al.* 2016). However, the present-day configuration of the EAIS is unlikely to have remained unchanged during the 6–13 Ma period, at least according to sheet and climate modelling predictions (e.g. DeConto & Pollard 2016) and previous marine sediment interpretations (Verma *et al.* 2014). In end-member deglaciated scenarios, for example, subglacial highlands will become a more probable sediment source region, while in a glaciated setting the subglacial basins will be a more probable source region due to enhanced erosion along the fast-flowing ice streams (e.g. Pandey *et al.* 2018).

The dominance of clinopyroxenes (especially pigeonite) and igneous amphiboles we identified in U1359 heavy minerals supports the presence of mafic rocks in the hinterland of the George V Coast region inferred as FLIP by Cook *et al.* (2013; Fig. 4). However, based on aeromagnetic interpretations, FLIP is compared to the Jurassic Ferrar Group, which is relatively well-exposed mostly as sills and rare dykes intruding into the Beacon Supergroup throughout the Transantarctic Mountains (e.g. Cook *et al.* 2013). We infer an extension of mafic rocks that are well-known in the formerly adjacent Gawler Craton of South Australia, at least within the northern WSB. In addition, diverse geochemical characteristics of clinopyroxene (Fig. 6) suggest multiple events of volcanic eruptions in the WSB. Hence, the FLIP evolution seems to be much more complex than previously inferred (e.g. Cook *et al.* 2013).

The Jurassic Ferrar Group is relatively well-exposed mostly as sills and rare dykes throughout the Transantarctic Mountains (e.g. Roland & Wöerner 1996). It intrudes into the Beacon Supergroup rocks of Devonian to Jurassic age (Barrett *et al.* 1986) and is in places overlain by thick Jurassic Kirkpatrick Basalt (Elliot *et al.* 1995).

Considering the MSZ-KSZ correlation, Mawson Craton in East Antarctica exhibits clear affinities with South Australia (e.g. Pierce *et al.* 2017). Coastal exposures of Terre Adélie Craton (e.g. Duclaux *et al.* 2008 and references therein) preserve key geological evidence for several orogenic and magmatic events that resemble the events recognized in Gawler Craton (Fitzsimons 2003, Aitken *et al.* 2014). The WSB may also contain Neoproterozoic red beds, potentially correlative to those identified in the Adelaide Rift Complex in Australia (Schmidt & Williams 2013). Mafic rift-related Neoproterozoic rocks also explain the distinct linear north-west to south-east-orientated aeromagnetic anomalies identified along the coastal regions of George V Land (Damaske *et al.* 2003). These anomalies lie at an angle to the more north to south-orientated Ferrar-related magnetic anomalies seen further south (Ferraccioli *et al.* 2009). Although these magnetic anomalies have previously been interpreted as Jurassic rift-related tholeiites along the coast of George V Land (Finn *et al.* 2006), we contend here that an alternative interpretation that these arise from older Neoproterozoic mafic sources is more probable. High-resolution aeromagnetic data over Gawler Craton and also the Coompana block in Australia (e.g. Wise *et al.* 2018) image linear north-west to south-east- to west-north-west to south-south-east-orientated magnetic anomalies over the 830–750 Ma Gairdner-Amata Dyke Swarm and inferred correlative rocks. Notably, these anomalies lie on strike, with the anomalies detected from much lower-resolution aeromagnetic data along the George V Coast (Damaske *et al.* 2003). Based on this correlation to the Australian counterpart, the possibility of extension of the Gairdner-Amata Dyke Swarm in the interior of the WSB is undeniable. The detrital pigeonite plot suggests the more complex variable composition of pigeonite if we compare it to the Ferrar dolerites,

suggesting more than one igneous volcanic event recorded in the interior of the WSB.

Crustal sagging at *c.* 800 Ma initiated the Centralian Superbasin followed by the deposition of marine and fluvial sands (Walter *et al.* 1995). A similar event would have caused the presence of low-grade metamorphic rocks in the interior of the WSB. The Tonian-aged monazite present in low-grade schist at U1359 of *c.* 830–750 Ma might represent the basement age for an older mafic volcanic activity that we propose to be the continuation of the Gairdner-Amata Dyke Swarm and the formation of the Adelaide Rift Complex in formerly adjacent Australia (Zhao *et al.* 1994). This hypothesis is further supported by the clinopyroxenes of U1359 that suggest sourcing from a putative tholeiitic magmatic source, which would be similar to that of the Gairdner giant dyke swarm (Zhao *et al.* 1994). The WSB region was not only affected by previously proposed early Cambrian basin formation and Jurassic tholeiitic magmatism (Ferraccioli *et al.* 2009), but also by older Neoproterozoic crustal extension and magmatism, which in turn heralded the break-up of the Rodinia supercontinent (e.g. Li *et al.* 2008). We suggest that the mafic rocks exposed in the WSB are much older than Jurassic, and their association with the Australian Gairdner-Amata Dyke Swarm is more probable than the earlier proposed association with the Jurassic Ferrar Group of the Transantarctic Mountains. This is further supported by the presence of low-geothermal-gradient signatures reported from the area (Fig. 10a; An *et al.* 2015). Younger magmatic rocks exposed in the Beacon Supergroup and the Ferrar Group in the Transantarctic Mountains exhibit high geothermal signatures (Fig. 10a, inset image).

Figure 10b shows the geology superimposed on the ADMAP-2 aeromagnetic data of the terrane, exhibiting high magnetic anomalies in the WSB (polygons with dashed black outline in Fig. 10b). Our new data suggest that the WSB includes low-grade Neoproterozoic metasedimentary basement rocks (*c.* 800 Ma) that are significantly older compared to the aeromagnetically inferred early Cambrian rocks, which have in turn been interpreted as reflecting a broad back-arc basin region affected by the Ross Orogen (Fig. 10b; Ferraccioli *et al.* 2009). This corroborates the orthopyroxene-garnet thermobarometer thermal conditions of $869 \pm 24°C$ at 8 kbar and, using the garnet and biotite thermometer, of $\sim587 \pm 17°C$ at 7 kbar. This supports a largely unexposed and at least low- to medium-grade metamorphosed Neoproterozoic terrane in the WSB region. The inferred low-grade metasediments could potentially resemble exposed low-grade metasedimentary rocks assigned to the western Wilson Terrane in Oates Land (Tessensohn & Henjes-Kunst 2005); however, the inferred *c.* 550–530 Ma depositional ages of these rocks are too young to be

related to the *c.* 800 Ma metasedimentary rocks inferred in this study. The unexposed metasediments in the WSB region are also too old to represent a continuation of the *c.* 550–520 Ma Kanmantoo Trough that was subsequently inverted during the Delamerian Orogen (Aitken *et al.* 2014, 2016). Whether these Precambrian metamorphic rocks are confined to the linear mountain ranges that flank the western WSB or also partially underlie the glacially over-deepened Western Basin and Central Basin (Fig. 10; Frederick *et al.* 2016), especially where Ninnis Glacier presently flows, is less clear, however.

The presence of 800–750 Ma signatures is further supported by detrital zircon geochronology in the sediments investigated from nearby Mertz Shelf-slope erratic detritals (e.g. Goodge & Fanning 2010, Veevers & Saeed 2011). Ages of 800 Ma are also reported from the Section Peak Formation and Ross Supergroup of adjacent North Victoria Land, which were clustered with either early Proterozoic ages *c.* 1200 Ma or with the Pan-African *c.* 500 Ma event (e.g. Paulsen *et al.* 2016). From detrital zircon records, *c.* 800 Ma ages ascribed usually either to Pb loss or not being part of the basin (e.g. Daczko *et al.* 2018, Tooze *et al.* 2020) merit more consideration. The limitations of the chemical geochronology of monazite smooth grain boundaries and the lack of cracks suggest the metamorphic origin of the monazite and not the detrital origin in the protolith, as well as indicating that the monazite has not experienced any mobility of REE phases and hence will provide accurate ages. The present work suggests the possibility of a 1100–500 Ma timeframe to preserve a complex history of crustal evolution, registering multiple thermo-tectonic events in the interior of the WSB. Globally, this is manifested in secular trends shown by a peak in zircon frequency at *c.* 700–800 Ma (Puetz *et al.* 2018), the collision ages of greenstone belts (Condie 1994) and the age distribution of eclogites and ultra-high-temperature metamorphic zones (Brown 2007). This is further supported by the newly emerged evidence of Tonian-Cryogenian (*c.* 700–800 Ma) metamorphic/magmatic events from Neoproterozoic shields worldwide (e.g. Africa: Itano *et al.* 2016, Sommer *et al.* 2017; China: Ge *et al.* 2016, Haozheng *et al.* 2020; East Antarctica: Jacobs *et al.* 2015, Arora *et al.* 2020, Sadiq *et al.* 2021 Gupta *et al.* 2022, and concordant zircon ages of Mikhalsky *et al.* 2020, Zong *et al.* 2020; India: Bose *et al.* 2016, Arora *et al.* 2017; southern Kazakhstan: Tretyakov *et al.* 2019). Although these ages are reported from almost every Gondwanan component, the events corresponding to *c.* 700–800 Ma (Tonian-Cryogenian) essentially remain enigmatic in the global orogenic context. Constraining the evolutionary history of Wilkes Land during the Neoproterozoic era is beyond the scope of our study.

Conclusions

1) Our sediment provenance study reveals previously unrecognized Precambrian metamorphic subglacial basement terrains. An upper amphibolite to granulite facies metamorphic belt is inferred to exist inland of correlative rock exposures in the Terre Adélie Craton, and it is linked based on the similarity in metamorphic grade to the Archaean and Palaeoproterozoic metamorphic rocks that are well-known in the formerly adjacent Gawler Craton in South Australia.

2) A unimodal age of 799 ± 13 Ma (Tonian) was estimated from a monazite grain found in the low-grade two-mica schist rock fragment, indicating a less recognized event in this sector.

3) The possibility of the presence of a Neoproterozoic metasedimentary basin and a younger magmatic terrane defines a complex geological set-up of the WSB.

Acknowledgements

Financial support

Competing interests

The authors declare that they have no known competing financial interests or personal relationships that could have appeared to influence the work reported in this paper.

Availability of data and material (data transparency)

The data are included in this publication in the form of Supplemental Tables S1–S13.

Author contributions

MP: execution, interpretation and writing - original draft preparation; NCP: conception, design and writing - review and editing; DA: interpretation and writing - review and editing; FF: interpretation and writing - review and editing; RG: writing, figures and editing; SJ: data analysis.

Supplemental material

Thirteen supplemental tables will be found at https://doi.org/10.1017/S0954102023000123.

References

AITKEN, A.R., BETTS, P.G., YOUNG, D.A., BLANKENSHIP, D.D., ROBERTS, J.L. & SIEGERT, M.J. 2016. The Australo-Antarctic Columbia to Gondwana transition. *Gondwana Research*, **29**, 136–152.

AITKEN, A.R., YOUNG, D.A., FERRACCIOLI, F., BETTS, P.G., GREENBAUM, J.S., RICHTER, T.G., *et al.* 2014. The subglacial geology of Wilkes Land, East Antarctica. *Geophysical Research Letters*, **141**, 2390–2400.

AN, M., WIENS, D.A., ZHAO, Y., FENG, M., NYBLADE, A.A., KANAO, M., *et al.* 2015. S-velocity model and inferred Moho topography beneath the Antarctic Plate from Rayleigh waves. *Journal of Geophysical Research - Solid Earth*, **120**, 359–383.

ARORA, D., PANT, N.C., SHARMA, S. & SADIQ, M. 2017. Inferring a Neoproterozoic orogeny preceding the Rodinia break-up in the Sirohi Group, NW India. *Special Publication of the Geological Society of London*, **457**, 319–338.

ARORA, D., PANT, N., PANDEY, M., CHATTOPADHYAY, A., GREENBAUM, J., SIEGERT, M., *et al.* 2020. Insights into geological evolution of Princess Elizabeth Land, East Antarctica - clues for continental suturing and breakup since Rodinian time. *Gondwana Research*, **84**, 260–283.

BARRETT, P.J., ELLIOT, D.H. & LINDSAY, J.F. 1986. The Beacon Supergroup (Devonian-Triassic) and Ferrar Group (Jurrasic) in the Beardmore Glacier Area, Antarctica. *Geology of the Central Transantarctic Mountains*, **36**, 339–428.

BASU, A. & MOLINAROLI, E. 1991. Reliability and application of detrital opaque Fe-Ti oxide minerals in provenance determination. *Special Publication of the Geological Society of London*, **57**, 55–65.

BATEMAN, R.M. & CATT, J.A. 2007. Provenance and palaeoenvironmental interpretation of superficial deposits, with particular reference to post-depositional modification of heavy mineral assemblages. *Developments in Sedimentology*, **58**, 151–188.

BHATTACHARYA, A., MOHANTY, L., MAJI, A., SEN, S.K. & RAITH, M. 1992. Non-ideal mixing in the phlogopite-annite binary: constraints from experimental data on Mg-Fe partitioning and a reformulation of the biotite-garnet geothermometer. *Contributions to Mineralogy and Petrology*, **111**, 87–93.

BIJL, P.K., HOUBEN, A.J., HARTMAN, J.D., PROSS, J., SALABARNADA, A., ESCUTIA, C. & SANGIORGI, F. 2018. Paleoceanography and ice sheet variability offshore Wilkes Land, Antarctica–Part 2: Insights from Oligocene–Miocene dinoflagellate cyst assemblages. *Climate of the Past* **14**(7), 1015–1033.

BISWAS, P., PANT, N.C., PANDEY, M. & SHRIVASTAVA, P.K. 2020. Sedimentological attributes and quartz microtexture in the levee sediments of a submarine channel in context of the East Antarctic

Ice Sheet fluctuations: a study from site U-1359 of IODP-318 Expedition. In D.K. Panday, M. Ravichandran & N. Nair, eds, *Dynamics of the Earth system: evolution, processes and interactions.* Berlin: Springer: 193–217.

Boger, S.D. 2011. Antarctica - before and after Gondwana. *Gondwana Research*, **19**, 335–371.

Bose, S., Das, K., Torimoto, J., Arima, M. & Dunkley, D.J. 2016. Evolution of the Chilka Lake granulite complex, northern eastern Ghats Belt, India: first evidence of ~780 Ma decompression of the deep crust and its implication on the India-Antarctica correlation. *Lithos*, **263**, 161–189.

Brown, M. 2007. Metamorphic conditions in orogenic belts: a record of secular change. *International Geology Review*, **49**, 193–234.

Condie, K.C. 1994. Greenstones through time. *Developments in Precambrian Geology*, **11**, 85–120.

Cook, C.P., Hemming, S.R., van de Flierdt, T., Davis, E.L., Williams, T., Galindo, A.L., *et al.* 2017. Glacial erosion of East Antarctica in the Pliocene: a comparative study of multiple marine sediment provenance tracers. *Chemical Geology*, **466**, 199–218.

Cook, C.P., van de Flierdt, T., Williams, T., Hemming, S.R., Iwai, M., Kobayashi, M., *et al.* 2013. Dynamic behaviour of the East Antarctic Ice Sheet during Pliocene warmth. *Nature Geoscience*, **6**, 765–769.

Daczko, N.R., Halpin, J.A., Fitzsimons, I.C. & Whittaker, J.M. 2018. A cryptic Gondwana-forming orogen located in Antarctica. *Scientific Reports*, **8**, 8371.

Damaske, D., Ferraccioli, F. & Bozzo, E. 2003. Aeromagnetic anomaly investigations along the Antarctic coast between Yule Bay and Mertz Glacier. *Terra Antartica*, **10**, 85–96.

Dasgupta, S., Sengupta, P., Guha, D. & Fukuoka, M. 1991. A refined garnet-biotite Fe-Mg exchange geothermometer and its application in amphibolites and granulites. *Contributions to Mineralogy and Petrology*, **109**, 130–377.

DeConto, R.M. & Pollard, D. 2016. Contribution of Antarctica to past and future sea-level rise. *Nature*, **531**, 591–597.

DeConto, R., Pollard, D. & Harwood, D. 2007. Sea ice feedback and Cenozoic evolution of Antarctic climate and ice sheets. *Paleoceanography*, **22**, 10.1029/2006PA001350.

Deer, W.A., Howie, R.A. & Zussman, J. 1992. *An introduction to the rock-forming minerals.* London: Longman Scientific and Technology, 712 pp.

Di Vincenzo, G., Talarico, F. & Kleinschmidt, G. 2007. An ^{40}Ar-^{39}Ar investigation of the Mertz Glacier area (George V Land, Antarctica): implications for the Ross Orogen-East Antarctic Craton relationship and Gondwana reconstructions. *Precambrian Research*, **152**, 93–118.

Duclaux, G., Rolland, Y., Ruffet, G., Ménot, R.P., Guillot, S., Peucat, J.J., *et al.* 2008. Superimposed Neoarchaean and Paleoproterozoic tectonics in the Terre Adélie Craton (East Antarctica): evidence from Th-U-Pb ages on monazite and ^{40}Ar/^{39}Ar ages. *Precambrian Research*, **167**, 316–338.

Elliot, D.H., Fleming, T.H., Haban, M.A. & Siders, M.A. 1995. Petrology and mineralogy of the Kirkpatrick basalt and Ferrar dolerite, Mesa range region, north Victoria Land, Antarctica. *Contributions to Antarctic Research IV*, **67**, 103–141.

Escutia, C., Cooper, A., Eittreim, S., Tanahashi, M., Ishihara, T., O'Brien, P., *et al.* 2011. *Wilkes Land glacial history: Cenozoic East Antarctic Ice Sheet evolution from Wilkes Land margin sediments.* IODP Proceedings Volume [318]. Tokyo: Integrated Ocean Drilling Program Management International, Inc.

Ferraccioli, F., Armadillo, E., Jordan, T., Bozzo, E. & Corr, H. 2009. Aeromagnetic exploration over the East Antarctic Ice Sheet: a new view of the Wilkes Subglacial Basin. *Tectonophysics*, **478**, 62–77.

Ferry, J.T. & Spear, F.S. 1978. Experimental calibration of the partitioning of Fe and Mg between biotite and garnet. *Contributions to Mineralogy and Petrology*, **66**, 113–117.

Finn, C.A., Goodge, J.W., Damaske, D. & Fanning, C.M. 2006. Scouting Craton's edge in paleo-Pacific Gondwana. In D.K. Fütterer, D. Damaske, G. Kleinschmidt, H. Miller & F. Tessensohn, eds, *Antarctica*. Berlin: Springer, 165–173.

Fitton, J.G. 1972. The genetic significance of almandine-pyrope phenocrysts in the calc-alkaline Borrowdale Volcanic Group, northern England. *Contributions to Mineralogy and Petrology*, **36**, 231–248.

Fitzsimons, I.C. 2003. Proterozoic basement provinces of southern and southwestern Australia, and their correlation with Antarctica. *Special Publication of the Geological Society of London*, **206**, 93–130.

Frederick, B.C., Young, D.A., Blankenship, D.D., Richter, T.G., Kempf, S.D., Ferraccioli, F. & Siegert, M.J. 2016. Distribution of subglacial sediments across the Wilkes Subglacial Basin, East Antarctica. *Journal of Geophysical Research - Earth Surface*, **121**, 790–813.

Fretwell, P., Pritchard, H.D., Vaughan, D.G., Bamber, J.L., Barrand, N.E., Bell, R., *et al.* 2013. Bedmap2: improved ice bed, surface and thickness datasets for Antarctica. *The Cryosphere*, **7**, 375–393.

Ge, X., Shen, C., Selby, D., Deng, D. & Mei, L. 2016. Apatite fission-track and Re-Os geochronology of the Xuefeng uplift, China: temporal implications for dry gas associated hydrocarbon systems. *Geology*, **44**, 491–494.

Gerner, E., Holgate, F.L. & Budd, A.R. 2010. OZTEMP: An updated map and database for predicting temperature at five kilometres depth in Australia. *GRC Transactions*, **34**, 345–346.

Gibson, G.M., Totterdell, J.M., White, L.T., Mitchell, C.H., Stacey, A.R., Morse, M.P. & Whitaker, A. 2013. Pre-existing basement structure and its influence on continental rifting and fracture zone development along Australia's southern rifted margin. *Journal of the Geological Society*, **170**, 365–377.

Golynsky, A.V., Ferraccioli, F., Hong, J.K., Golynsky, D.A., von Frese, R.R., Young, D.A., *et al.* 2018. New magnetic anomaly map of the Antarctic. *Geophysical Research Letters*, **45**, 6437–6449.

Goodge, J.W. 2007. Proxies of the East Antarctic shield: composition and age of ice-covered basement from sedimentary and glacial provenance. In *Antarctica: a keystone in a changing world. International Symposium on Antarctic Earth Sciences,* 10th online proceedings. Reston, VA, US Geological Survey, Abstract 132.

Goodge, J.W. & Fanning, C.M. 2010. Composition and age of the East Antarctic Shield in eastern Wilkes Land determined by proxy from Oligocene–Pleistocene glaciomarine sediment and Beacon Supergroup sandstones, Antarctica. *GSA Bulletin*, **122**, 1135–1159.

Green, T.H. & Ringwood, A.E. 1968. Origin of garnet phenocrysts in calc-alkaline rocks. *Contributions to Mineralogy and Petrology*, **18**, 163–174.

Greenwood, N.N. & Earnshaw, A. 1998. Copper, silver and gold. *Chemistry of the Elements*, **28**, 1178–1190.

Gupta, R., Pandey, M., Arora, D., Pant, N.C. & Rao, N.C. 2022. Evincing the presence of a trans-Gondwanian mobile belt in the interior of the Princess Elizabeth Land, East Antarctica: insights from offshore detrital sediments, rock fragments, and monazite geochronology. *Geological Journal*, **57**, 10.1002/gj.4430.

Hamer, R.D. & Moyes, A.B. 1982. Composition and origin of garnet from the Antarctic Peninsula Volcanic Group of Trinity Peninsula. *Journal of the Geological Society*, **139**, 713–720.

Hansen, M.A., Passchier, S., Khim, B.K., Song, B. & Williams, T. 2015. Threshold behavior of a marine-based sector of the East Antarctic Ice Sheet in response to early Pliocene ocean warming. *Paleoceanography*, **30**, 789–801.

Haozheng, W., Oscar, L., Huafeng, Z., Hong, Z., Xi, C. & Mingguo, Z. 2020. Recognition and significance of *c.* 800 Ma upper amphibolite to granulite facies metamorphism in metasedimentary rocks from the NW margin of the Yangtze Block. *Journal of the Geological Society*, **177**, 424–441.

HARLEY, S.L., FITZSIMONS, I.C. & ZHAO, Y. 2013. Antarctica and supercontinent evolution: historical perspectives, recent advances and unresolved issues. *Special Publication of the Geological Society of London*, **383**, 1–34.

HEROLD, N., HUBER, M. & MÜLLER, R.D. 2011. Modeling the Miocene climatic optimum. Part I: land and atmosphere. *Journal of Climate*, **24**, 6353–6372.

ITANO, K., IIZUKA, T., CHANG, Q., KIMURA, J.I. & MARUYAMA, S. 2016. U-Pb chronology and geochemistry of detrital monazites from major African rivers: constraints on the timing and nature of the Pan-African Orogeny. *Precambrian Research*, **282**, 139–156.

JACOBS, J., ELBURG, M., LÄUFER, A., KLEINHANNS, I.C., HENJES-KUNST, F., ESTRADA, S., *et al.* 2015. Two distinct Late Mesoproterozoic/Early Neoproterozoic basement provinces in central/eastern Dronnning Maud Land, East Antarctica: the missing link, 15–21°E. *Precambrian Research*, **265**, 249–272.

JORDAN, T.A., FERRACCIOLI, F., VAUGHAN, D.G., HOLT, J.W., CORR, H., BLANKENSHIP, D.D. & DIEHL, T.M. 2010. Aerogravity evidence for major crustal thinning under the Pine Island Glacier region (West Antarctica). *GSA Bulletin*, **122**, 714–726.

LAMARQUE, G., BASCOU, J., MAURICE, C., COTTIN, J.Y., RIEL, N. & MÉNOT, R.P. 2016. Microstructures, deformation mechanisms and seismic properties of a Palaeoproterozoic shear zone: the Mertz Shear Zone, East-Antarctica. *Tectonophysics*, **680**, 174–191.

LEAKE, B.E. 1965. The relationship between tetrahedral aluminium and the maximum possible octahedral aluminum in natural calciferous and subcalciferous amphiboles. *American Mineralogist*, **50**, 843–851.

LEAKE, B.E., WOOLLEY, A.R., ARPS, C.E., BIRCH, W.D., GILBERT, M.C., GRICE, J.D., *et al.* 1997. Nomenclature of amphiboles; report of the Subcommittee on Amphiboles of the International Mineralogical Association Commission on new minerals and mineral names. *Mineralogical Magazine*, **61**, 295–310.

LETERRIER, J., MAURY, R.C., THONON, P., GIRARD, D. & MARCHAL, M. 1982. Clinopyroxene composition as a method of identification of the magmatic affinities of paleo-volcanic series. *Earth and Planetary Science Letters*, **59**, 139–154.

LI, Z.X., BOGDANOVA, S., COLLINS, A.S., DAVIDSON, A., DE WAELE, B., ERNST, R.E., *et al.* 2008. Assembly, configuration, and break-up history of Rodinia: a synthesis. *Precambrian Research*, **160**, 179–210.

LINDSLEY, D.H. & ANDERSEN, D.J. 1983. A two-pyroxene thermometer. *Journal of Geophysical Research - Solid Earth*, **88**, A887–A906.

LUDWIG, K.R. 2003. *User's manual for* Isoplot 3.00, *a geochronological toolkit for Microsoft* Excel. Berkeleky, CA: Berkeley Geochronology Center, 25–32.

MANGE, M.A. & MORTON, A.C. 2007. Geochemistry of heavy minerals. *Developments in Sedimentology*, **58**, 345–391.

MANGE, M.A. & WRIGHT, D.T., *eds.* 2007. *Heavy minerals in use.* Amsterdam: Elsevier, 780 pp.

MATSUOKA, K., SKOGLUND, A., ROTH, G., DE POMEREU, J., GRIFFITHS, H., HEADLAND, R., *et al.* 2021. *Quantarctica*, an integrated mapping environment for Antarctica, the Southern Ocean, and sub-Antarctic islands. *Environmental Modelling & Software*, **140**, 105015.

MCMULLEN, K., DOMACK, E., LEVENTER, A., OLSON, C., DUNBAR, R., & BRACHFELD, S. 2006. Glacial morphology and sediment formation in the Mertz Trough, East Antarctica. *Palaeogeography, Palaeoclimatology, Palaeoecology*, **231**, 169–180.

MÉNOT, R.P., DUCLAUX, G., PEUCAT, J.J., ROLLAND, Y., GUILLOT, S., FANNING, M., *et al.* 2007. Geology of the Terre Adélie Craton (135–146 E). In *Antarctica: a keystone in a changing world. International Symposium on Antarctic Earth Sciences,* 10*th online proceedings.* Reston, VA, US Geological Survey, Short Research Paper 048.

MIKHALSKY, E.V., ANDRONIKOV, A.V., LEITCHENKOV, G.L. & BELYATSKY, B.V. 2020. The age of continental crust in the northern Prince Charles mountains (East Antarctica) as evidenced by zircon xenocrysts from cretaceous alkaline-ultramafic rocks. *Lithos*, **368**, 105599.

MONTEL, J.M., FORET, S., VESCHAMBRE, M., NICOLLET, C. & PROVOST, A. 1996. Electron microprobe dating of monazite. *Chemical Geology*, **131**, 37–53.

MORIMOTO, N. 1988. Nomenclature of pyroxenes. *Mineralogy and Petrology*, **39**, 55–76.

MORRISSEY, L.J., PAYNE, J.L., HAND, M., CLARK, C., TAYLOR, R., KIRKLAND, C.L. & KYLANDER-CLARK, A. 2017. Linking the Windmill Islands, East Antarctica and the Albany-Fraser Orogen: insights from U-Pb zircon geochronology and Hf isotopes. *Precambrian Research*, **293**, 131–149.

MORTON, A., HALLSWORTH, C. & CHALTON, B. 2004. Garnet compositions in Scottish and Norwegian basement terrains: a framework for interpretation of North Sea sandstone provenance. *Marine and Petroleum Geology*, **21**, 393–410.

NAISH, T., POWELL, R., LEVY, R., WILSON, G., SCHERER, R., TALARICO, F., *et al.* 2009. Obliquity-paced Pliocene West Antarctic Ice Sheet oscillations. *Nature*, **458**, 322–328.

OREJOLA, N., PASSCHIER, S. & IODP EXPEDITION 318 SCIENTISTS. 2014. Sedimentology of lower Pliocene to upper Pleistocene diamictons from IODP site U1358, Wilkes Land margin, and implications for East Antarctic Ice Sheet dynamics. *Antarctic Science*, **26**, 183–192.

PANDEY, M., PANT, N.C., ARORA, D. & GUPTA, R. 2021. A review of Antarctic ice sheet fluctuations records during Cenozoic and its cause and effect relation with the climatic conditions. *Polar Science*, **30**, 100720.

PANDEY, M., PANT, N.C., BISWAS, P., SHRIVASTAVA, P.K., JOSHI, S. & NAGI, N. 2018. Heavy mineral assemblage of marine sediments as an indicator of provenance and East Antarctic Ice Sheet fluctuations. *Special Publication of the Geological Society of London*, **61**, 95–111.

PANT, N.C., BISWAS, P., SHRIVASTAVA, P.K., BHATTACHARYA, S., VERMA, K. & PANDEY, M. 2013. Expedition I. Provenance of Pleistocene sediments from site U1359 of the Wilkes Land IODP Leg 318 - evidence for multiple sourcing from the East Antarctic Craton and Ross Orogen. *Special Publication of the Geological Society of London*, **381**, 277–297.

PANT, N.C., KUNDU, A., JOSHI, S., DEY, A., BHANDARI, A. & JOSHI, A. 2009. Chemical dating of monazite: testing of an analytical protocol against independently dated standards. *Indian Journal of Geosciences*, **63**, 311–318.

PAULSEN, T.S., DEERING, C., SLIWINSKI, J., BACHMANN, O. & GUILLONG, M. 2016. Detrital zircon ages from the Ross Supergroup, north Victoria Land, Antarctica: implications for the tectonostratigraphic evolution of the Pacific-Gondwana margin. *Gondwana Research*, **35**, 79–96.

PIERCE, E.L., VAN DE FLIERDT, T., WILLIAMS, T., HEMMING, S.R., COOK, C.P. & PASSCHIER, S. 2017. Evidence for a dynamic East Antarctic Ice Sheet during the mid-Miocene climate transition. *Earth and Planetary Science Letters*, **478**, 1–13.

POLLARD, D. & DECONTO, R.M. 2009. Modelling West Antarctic Ice Sheet growth and collapse through the past five million years. *Nature*, **458**, 329–332.

POLLARD, D., DECONTO, R.M. & ALLEY, R.B. 2015. Potential Antarctic ice sheet retreat driven by hydrofracturing and ice cliff failure. *Earth and Planetary Science Letters*, **412**, 112–121.

PUETZ, S.J., GANADE, C.E., ZIMMERMANN, U. & BORCHARDT, G. 2018. Statistical analyses of global U-Pb database 2017. *Geoscience Frontiers*, **9**, 121–145.

REED, J.B. & BUCKLEY, A. 1996. Virtual WDS. *In* D. BENOIT, J.-F. BRESSE, L. VAN'T DACK, H. WERNER & J. WERNISCH, *eds, Microbeam and nanobeam analysis.* Berlin: Springer, 479–483.

REID, A.J. & HAND, M. 2012. Mesoarchean to mesoproterozoic evolution of the southern Gawler Craton, South Australia. *Episodes*, **35**, 216–225.

RIETMEIJER, F.J. 1983. Chemical distinction between igneous and metamorphic orthopyroxenes especially those coexisting with Ca-rich clinopyroxenes: a re-evaluation. *Mineralogical Magazine*, **47**, 143–151.

RIGNOT, E., MOUGINOT, J. & SCHEUCHL, B. 2011. Ice flow of the Antarctic ice sheet. *Science*, **333**, 1427–1430.

ROBINSON, P., ROSS, M., NORD, G.L., SMYTH, J.R. & JAFFE, H.W. 1977. Exsolution lamellae in augite and pigeonite; fossil indicators of lattice parameters at high temperature and pressure. *American Mineralogist*, **62**, 857–873.

RODRIGUEZ-GONZALEZ, A., FERNANDEZ-TURIEL, J.L., PEREZ-TORRADO, F.J., PARIS, R., GIMENO, D., CARRACEDO, J.C. & AULINAS, M. 2012. Factors controlling the morphology of monogenetic basaltic volcanoes: the Holocene volcanism of Gran Canaria (Canary Islands, Spain). *Geomorphology*, **136**, 31–44.

ROLAND, N.W. & WOERNER, G.E. 1996. Kirkpatrick flows and associated pyroclastics: new occurrences, definition, and aspects of a Jurassic Transantarctic Rift. *Geologisches Jahrbuch Reihe B*, **89**, 97–122.

SABEEN, H.M., RAMANUJAM, N. & MORTON, A.C. 2002. The provenance of garnet: constraints provided by studies of coastal sediments from southern India. *Sedimentary Geology*, **152**, 279–287.

SADIQ, M., DHARWADKAR, A., ROY, S.K., ARORA, D., SHAH, M.Y. & BHANDARI, A. 2021. Thermal evolution of mafic granulites of Princess Elizabeth Land, East Antarctica. *Polar Science*, **30**, 100641.

SCHER, H.D., BOHATY, S.M., ZACHOS, J.C. & DELANEY, M.L. 2011. Two-stepping into the icehouse: East Antarctic weathering during progressive ice-sheet expansion at the Eocene–Oligocene transition. *Geology*, **39**, 383–386.

SCHMIDT, P.W. & WILLIAMS, G.E. 2013. Anisotropy of thermoremanent magnetisation of Cryogenian glaciogenic and Ediacaran red beds, South Australia: Neoproterozoic apparent or true polar wander? *Global and Planetary Change*, **110**, 289–301.

SCHNEIDERMAN, J.S. 1995. Detrital opaque oxides as provenance indicators in River Nile sediments. *Journal of Sedimentary Research*, **65**, 668–674.

SCHÜSSLER, U., BRÖCKER, M., HENJES-KUNST, F. & WILL, T. 1999. P-T-t evolution of the Wilson Terrane metamorphic basement at Oates Coast, Antarctica. *Precambrian Research*, **93**, 235–258.

SOMMER, H., KRÖNER, A. & LOWRY, J. 2017. Neoproterozoic eclogite- to high-pressure granulite-facies metamorphism in the Mozambique belt of east-central Tanzania: a petrological, geochemical and geochronological approach. *Lithos*, **284**, 666–690.

TALARICO, F. & KLEINSCHMIDT, G. 2003. The Mertz Shear Zone (George V Land): implications for Australia/Antarctica correlations and East Antarctic Craton/Ross Orogen relationships. *Terra Antarctica*, **9**, 149–153.

TAUXE, L., STICKLEY, C.E., SUGISAKI, S., BIJL, P.K., BOHATY, S.M., BRINKHUIS, H., *et al.* 2012. Chronostratigraphic framework for the IODP Expedition 318 cores from the Wilkes Land Margin: constraints for paleoceanographic reconstruction. *Paleoceanography and Paleoclimatology*, **27**, 10.1029/2012PA002308.

TESSENSOHN, F. & HENJES-KUNST, F. 2005. Northern Victoria Land terranes, Antarctica: far-travelled or local products? *Special Publication of the Geological Society of London*, **246**, 275–291.

TOOZE, S., HALPIN, J.A., NOBLE, T.L., CHASE, Z., O'BRIEN, P.E. & ARMAND, L. 2020. Scratching the surface: a marine sediment provenance record from the continental slope of central Wilkes Land, East Antarctica. *Geochemistry, Geophysics, Geosystems*, **21**, 2020GC009156.

TRETYAKOV, A.A., PILITSYNA, A.V., DEGTYAREV, K.E., SALNIKOVA, E.B., KOVACH, V.P., LEE, H.Y., *et al.* 2019. Neoproterozoic granitoid magmatism and granulite metamorphism in the Chu-Kendyktas terrane (southern Kazakhstan, Central Asian Orogenic Belt): zircon dating, Nd isotopy and tectono-magmatic evolution. *Precambrian Research*, **332**, 105397.

VEEVERS, J.J. & SAEED, A. 2011. Age and composition of Antarctic bedrock reflected by detrital zircons, erratics, and recycled microfossils in the Prydz Bay-Wilkes Land-Ross Sea-Marie Byrd Land sector (70–240 E). *Gondwana Research*, **20**, 710–738.

VERMA, K., BHATTACHARYA, S., BISWAS, P., SHRIVASTAVA, P.K., PANDEY, M. & PANT, N.C. 2014. Clay mineralogy of the ocean sediments from the Wilkes Land margin, East Antarctica: implications on the paleoclimate, provenance and sediment dispersal pattern. *International Journal of Earth Sciences*, **103**, 2315–2326.

WALTER, M.R., VEEVERS, J.J., CALVER, C.R. & GREY, K. 1995. Neoproterozoic stratigraphy of the Centralian Superbasin, Australia. *Precambrian Research*, **73**, 173–195.

WEAVER, S.D., BRADSHAW, J.D. & LAIRD, M.G. 1984. Geochemistry of Cambrian volcanics of the Bowers Supergroup and implications for the Early Palaeozoic tectonic evolution of northern Victoria Land, Antarctica. *Earth and Planetary Science Letters*, **68**, 128–140.

WISE, T., DUTCH, R., PAWLEY, M., FOSS, C. & THIEL, S. 2018. Building the Coompana province. *MESA Journal*, **88**, 25–37.

ZHAO, J.X., MCCULLOCH, M.T. & KORSCH, R.J. 1994. Characterisation of a plume-related ~800 Ma magmatic event and its implications for basin formation in central-southern Australia. *Earth and Planetary Science Letters*, **121**, 349–367.

ZONG, S., REN, L. & WU, M. 2020. Grenvillian metamorphism of sillimanite-garnet feldspar paragneiss in the Larsemann Hills, East Antarctica and tectonic implications. *Acta Petrologica Sinica*, **36**, 1931–1944.